



Influence of Binding Energies on Required Process Conditions in Aerosol Deposition

Bahman Daneshian¹ · Frank Gärtner² · Hamid Assadi³ · Daniel Höche⁴ · Thomas Klassen² · Wolfgang E. Weber¹

Submitted: 3 June 2024 / in revised form: 16 August 2024 / Accepted: 13 September 2024 / Published online: 18 October 2024
© The Author(s) 2024

Abstract With the high interest in aerosol deposition in order to form high-quality coatings by solid-state impact, there is an increasing demand for developing general guidelines to estimate needed particle velocities and thus process parameter sets for successful deposition of ceramic materials. By using modeling approaches, rather different material properties in first instance can be expressed in terms of binding energies. Needed velocities for possible bonding can then derived by impact simulations and compared to experimental results from the literature. In order to study the role of binding energy on the impact behavior of ceramic particles in aerosol deposition, a molecular dynamics study is presented. Single-particle impacts are simulated for a range of binding energies, particle sizes and impact velocities. The results show that increasing the binding energy from 0.22 to 0.96 eV results in up to three times higher characteristic velocities corresponding to the threshold of bonding or grain size-dependent fragmentation of the particles. However, regardless of the binding energy, exceeding the characteristic velocities results in a similar deformation and fragmentation pattern.

This allows for a general representation of the impact behavior as a function of normalized impact velocity for different ceramic materials. Apart from dealing with prerequisites for bonding of different materials by aerosol deposition, this study could also be generally relevant to the high-velocity deformation behavior of ceramics with different grain sizes.

Keywords aerosol deposition · binding energy · molecular dynamics · nanoparticle

Introduction

The aerosol deposition method, abbreviated as AD, is a promising solid-state spraying technique for building up ceramic coatings on different substrate materials, such as metals, ceramics and even polymers (Ref 1-3). In AD, submicron to micron size ceramic particles, i.e., from 200 nm to 5 µm (Ref 4, 5), are accelerated in a carrier gas flow of 1-40 L/min (Ref 4-6) to velocities of 100-600 m/s and then impact on the substrate in a vacuum chamber (Ref 4). In the ideal case, this technology allows the processing of ceramic coatings to reach similar or even better properties in their nanocrystalline state than a respective bulk material (Ref 3, 4).

Early work in AD (Ref 1-3) reported different impact velocities for coating formation by investigating different ceramic powders. The required impact velocity to create such coatings increases with increasing sintering temperature for a particular ceramic material (Ref 3). For example, it is reported that alpha-alumina particles, as a hard material (YOUNG's modulus $E \approx 370$ GPa), require velocities of 150-500 m/s to create a coating with acceptable hardness. Whereas the lead zirconate titanate (PZT) powders as

✉ Bahman Daneshian
daneshba@hsu-hh.de

¹ Chair of Structural Analysis, Helmut Schmidt University/ University of the Federal Armed Forces, Holstenhofweg 85, 22043 Hamburg, Germany

² Institute for Materials Technology, Helmut Schmidt University/University of the Federal Armed Forces, Holstenhofweg 85, 22043 Hamburg, Germany

³ Brunel Centre for Advanced Solidification Technology, Brunel University London, Kingston Lane, Uxbridge UB8 3PH, UK

⁴ Institute of Surface Science, Helmholtz-Zentrum Hereon, Max-Planck-Straße 1, 21502 Geesthacht, Germany

soft ceramics ($E \approx 70$ GPa) require lower impact velocities, i.e., 100–300 m/s, to form coatings with an acceptable hardness. Values of such impact velocities for some ceramics such as alpha-alumina, PZT, Fe_2O_3 , AlN and MgB_2 were first reported by Akedo (Ref 3). According to Hanft et al. (Ref 4) and Akedo (Ref 2), a threshold velocity exists for depositing specific materials by AD. Apart from ceramic powder properties, the threshold velocity was also shown to be dependent on the type of substrate material (Ref 3, 4). In addition, AD experiments and simulations by Kwon et al. (Ref 5) on 1 μm single-crystalline silicon dioxide and alpha-alumina revealed that coating formation would be successful if the velocities of the particles were equal to and higher than 300 and 400 m/s, respectively.

Besides Kwon's and Akedo's studies (Ref 3, 5), some hints on the dependency of the needed velocity for bonding of different ceramic types were given by molecular dynamics (MD) simulations (Ref 7–9) and analytical models (Ref 10). These studies (Ref 7–10) showed that the needed velocity for bonding, i.e., the threshold velocity, is independent of the particle size but depends on the material properties such as density and YOUNG's modulus (Ref 10). The suggested threshold velocity model (Ref 10) agreed well with experimental data for silicon dioxide and alpha-alumina particles (Ref 5, 10). In summary, the understanding of the influences of material type and properties on the threshold velocity in AD appears to be an essential prerequisite for the successful design of the spraying process for a wide range of ceramic materials (Ref 11).

Previous publications already describe the general features of AD coatings (Ref 3, 4, 12) for different types of ceramic materials. These studies showed that despite the different hardness of initial ceramic powders, all coatings that are successfully formed by AD show similar microstructures. These dense and pore-free coatings consist of 10–30 nm grains (Ref 3) with intimate bonding to the substrate. To some extent, AD coatings on the basis of softer materials are more prone to show flow lines or waves as an indication of plastic deformation and flattening (Ref 3, 4, 12). The overall coating appearance in AD is also influenced by substrate materials and initial topographies (Ref 4, 7). The previous work reports predominant crater formation by larger particle impact on softer material substrates such as copper and glass. To a certain extent, the substrate properties influence overall AD coating appearance, indicating a trend that harder and rougher substrates cause rougher coating surfaces (Ref 13). Despite extensive research on the effects of particle material types and sizes as well as substrate properties on success in building up coatings by AD, so far, no uniform description of associated bonding mechanisms could be derived.

Previous MD simulations revealed that sufficiently high particle velocities in AD could cause plastic deformation and, within certain velocity regimes, enable bonding (Ref 8–10). Too high velocities or large particle sizes promote fracture. In this view, following the collision between the particle and the substrate, three distinct structures may be formed, depending on the particle's impact behavior: (i) A small "portion" of particles remains on the substrate, primarily because most other particles rebound; (ii) a "cone/triangle-shaped" area remains on the substrate following the particle's global (bulk) fragmentation behavior or propagation of larger cracks and (iii) "fragmented" parts following the particle's localized (inner) deformation behavior by multiple smaller cracks or plastic deformation. Increased overall deposition efficiency in AD is associated with forming a highly plastically deformed cone-shaped area at the lower part of the impacted particle close to the substrate interface. The cone-shaped region is surrounded by shear cracks. In addition, meridional cracks could be formed.

The plastically deformed region plays a key role with respect to particle bonding, it is essential to understand possible influences of mechanical properties on (i) sizes of the cone-shaped region, (ii) densities and lengths of surrounding cracks and even possibly (iii) grain refinement within this cone region. With respect to particle fracture and their role in particle fragmentation, influences of mechanical particle properties on the formation and growth of meridional and shear cracks should be derived. Moreover, MD modeling has provided detailed insights into plastic deformation and shear localization in ceramic particles during AD, surpassing the capabilities of current experimental methods and other modeling approaches (Ref 9, 10, 14, 15).

The previous research of the authors on molecular dynamics modeling of aerosol deposition has evolved from examining the impact behavior of brittle nanoparticles to exploring the complex interplay between particle size, velocity and mechanical parameters. Initially, by using a modified Lennard–Jones model, single-crystalline brittle nanoparticles of a generic material that impact onto rigid substrates were investigated over a rather narrow size regime to assess influences by velocity onto changes in impact behavior (Ref 7). These simulations revealed that nanoparticles could deform without fragmenting if their size was below a critical threshold, sometimes leading to polycrystallization and bonding to the substrate. Based on these findings, the research was expanded to tune bonding energies for simulating Anatase TiO_2 as a model system and to include ceramic particles across a broader size range (10–300 nm). The results showed that only sufficiently small particles bonded without fragmentation, whereas larger particles did not (Refs 8, 9). Mainly focusing on

Anatase TiO₂, the following work (Ref 10) revealed plastic deformation as one key factor for particle bonding and found hints on grain size reduction upon impact. Moreover, analytical models were developed in order to predict conditions for bonding or fragmentation and influences on transitions in between by particle sizes, velocities and mechanical properties. However, despite incorporating mechanical properties into the parameterization of these models, a systematic study on respective influences by impact simulation was not supplied, nor possibly associated heat generation by plastic deformation upon impact. Thus, the present paper now addresses the gaps in understanding by providing a more detailed simulation analysis of the influence of mechanical properties on particle impact behavior, associated velocity dependent transitions to fragmentation and plasticity related heat generation during impact.

The current study also aims to derive more general trends to describe conditions that enable successful particle bonding of different ceramic materials by AD using molecular dynamics. To encompass different ceramic materials within the simulations, modifications were made to the Lennard–Jones potential, yielding artificial brittle materials. By manipulating the binding energy parameter in the modified Lennard–Jones potential (M-LJ), the mechanical properties of a wide range of ceramics commonly used in the AD process were emulated. Subsequently, the study of impact behaviors focused on analyzing (i) deformation patterns, (ii) fracture patterns, (iii) temperature evolution and (iv) possible grain refinement within a single particle. After pre-adjusting different binding energies, the individual investigations involved analysis under varied (i) impact velocities and (ii) particle sizes. The aim was to gain insights into the diverse aspects of the AD process, including the behavior and properties of ceramic particles with different characteristics.

It should also be mentioned that the simplified two-dimensional (2D) model with the modified Lennard–Jones potential used in this study may restrict the precise data extraction. For instance, 2D modeling has less geometrical freedom for deformation than 3D, potentially underestimating deformation and shifting bonding and fragmentation behaviors to higher impact velocities. However, the 2D approach significantly reduces computational time, allowing the simulation of real-size particles in AD. Additionally, the modified Lennard–Jones potential enables analysis of the binding energy of various ceramic materials at consistent impact velocities and particle sizes. Despite its limitations, the 2D model offers valuable insights into trends, justifying its use in this research.

Methods

Modeling and Model Adjustments

In this study, the molecular dynamics (MD) method was employed to simulate tensile tests and particle impact phenomena by means of a simplified two-dimensional (2D) model. The simplified 2D approach was used to reduce computational time for a rather wide range of material properties and parameter screening. Despite the missing accuracy, such an attempt should nevertheless allow for deriving relevant trends. The MD simulations were all performed using LAMMPS software (Ref 16). In these 2D simulations by using LAMMPS, the Z-components of atomic velocities and atomic forces are set to zero after every timestep automatically in order to provide a plain strain condition. We are aware that with respect to three-dimensional (3D) simulations, the currently used 2D approach will suffer from (i) missing influences by molecular structure and possible slip systems and (ii) less degree of freedom during deformation. Nevertheless, it remains a crucial strategy to model larger-sized brittle particles in AD using molecular dynamics.

The material brittleness is considered by a M-LJ potential (M-LJ) in Eq. 1 as given (Ref 8, 10, 13).

$$M - LJ = \begin{cases} \varepsilon = \left[\left(\frac{\sigma}{r} \right)^{12} - \left(\frac{\sigma}{r} \right)^6 \right] & \text{if } \frac{r}{\sigma} < r_c \\ 0 & \text{if } \frac{r}{\sigma} \geq r_c \end{cases} \quad (\text{Eq 1})$$

In this equation, r is the atomic distance between two atoms, r_c is the dimensionless cut-off radius and ε and σ are the characteristic energy and length parameters, respectively. In contrast with the usual Lennard–Jones description (Ref 17), the cut-off radius r_c equal to 3.345 Å (1.5 σ) was induced here in order to consider material brittleness within the model (Ref 8, 10). Then, different material properties were achieved by systematically varying the binding energies to 0.22, 0.45, 0.65 and 0.96 eV using the energy parameter (ε) in Eq. 1, while keeping the length parameter (σ) equal to 2.23 Å in this equation. This value was chosen based on prior analyses to reflect material properties comparable to those of ceramics used in AD, ensuring consistency throughout the study. The individual binding energies were selected according to previous work and pre-analyses by simulating tensile tests in order to gain realistic YOUNG's moduli data, as later given in the results (Ref 8, 10).

In the tensile test simulation section, simulations of tensile tests are conducted to evaluate YOUNG's moduli of the different model materials and to ensure brittleness under the varied binding energies. The determination of YOUNG's moduli provides a correlation to real material

properties as associated with the different binding energies. This should allow for a comparison with ceramic materials that are in use by AD.

Tensile Test Simulations

In principle, the YOUNG's modulus can be calculated from the curvature of the MLJ potential function at the equilibrium point. However, such an approach would not meet all needs of the current adjustments of material properties. Here, tensile test modeling was performed to evaluate material aspects with respect to material brittleness and the YOUNG's modulus associated with the chosen binding energy. The first derivative of the potential interatomic distance curve provides information about interatomic forces, but YOUNG's modulus is derived from the stress–strain relationship obtained from tensile tests or simulations. YOUNG's modulus reflects the material stiffness and is calculated as the ratio of stress to strain. By using tensile modeling, the material response under applied stress can be derived, which offers a more nuanced understanding of its mechanical properties.

Within the initial atomic configurations in a single-crystalline close-packed (11) fcc plane, the 2D tensile test geometry was created by cuts according to $\langle 10 \rangle$ and $\langle 01 \rangle$ crystallographic orientations. Each tensile test model was rectangular with a size of $35 \text{ nm} \times 100 \text{ nm}$. The length measurements in this study rely on the equilibrium distance between two atoms in the M-LJ potential, which is set to 2.5 \AA and corresponds to $2^{1/6} \sigma$. The principle of geometric arrangement is given in Fig. 1. In order to simulate a tensile test analogous to a macroscopic experiment, the deformation was applied in opposite directions in the X -axis, i.e., left and right sides of the simulation box in Fig. 1(a), with a constant velocity of 0.1 m/s . The periodic boundary conditions were added to the simulation box in the X and Y axes to allow the atoms to

move freely in these directions and thus avoid influences of the model's size on the stress–strain curves.

During the straining simulations, the tensile test models were equilibrated at room temperature (300 K) to consider the close to real bulk temperatures. For this purpose, the tensile test simulations were run under the Canonical ensemble (Ref 18), where the simulation box was in thermal equilibrium with a heat bath at 300 K , using the Velocity Verlet algorithm (Ref 17) and time steps of $5 \times 10^{-15} \text{ s}$.

To determine stress–strain curves, the atomic stress tensors in the X -axis were summed over all atoms inside the tensile test simulation box. In MD, the atomic stress tensor for an atom i , i.e., $\sigma_{ab}(i)$, is calculated based on the kinetic energy and the virial pressure contribution expressed through Eqs. (2) and (3), as given by (Ref 16). Herein, m denotes the atomic mass, while v_a and v_b represent atomic velocities in either the X - or Y -axis and could also be identical to each other.

$$\sigma_{ab}(i) = -m(i) \cdot v_a(i) \cdot v_b(i) - W(r_c) \quad (\text{Eq 2})$$

$$W(r_c) = \frac{1}{2} \sum_{i=1}^{N_p} (r(i) \cdot F(i)) \quad (\text{Eq 3})$$

The virial pressure contribution in Eq. 2, i.e., $W(r_c)$, is defined as given by Eq. 3, where $r(i)$ is the interatomic distance between atom i and its neighboring atom within the defined cut-off radius, i.e., r_c , and $F(i)$ denotes the interatomic force acting on atom i owing to its interaction with the neighboring atom within the cut-off radius (Ref 18). N_p also refers to the number of atoms existing inside the cut-off radius.

Particle Impact Simulations

The 2D particle impact models were created by cuts from a close-packed (11) and single-crystalline fcc plane.

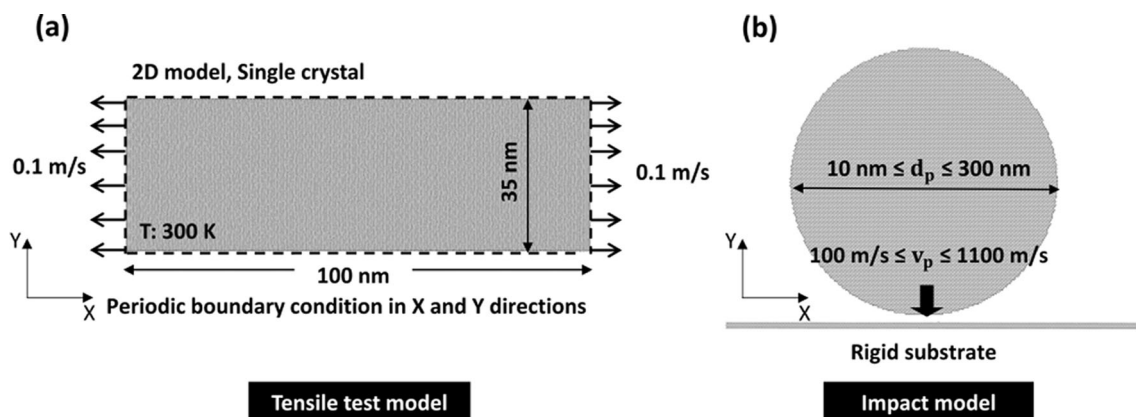


Fig. 1 Model set up for (a) tensile test and (b) particle impact simulation

This simplification follows previous modeling approaches for AD (Ref 8-10) to facilitate the analysis of deformation and fragmentation inside the single-crystalline particles. In practice, polycrystalline particles are typically used in AD due to feedstock availability (Ref 20). However, the crystalline grain sizes in these powders are usually quite large, up to several hundred nanometers, because smaller grains often hinder coating formation in AD (Ref 3, 20). In some cases, studies have shown that single-crystalline alpha-alumina particles can successfully form coatings in AD (Ref 21). As indicated by Kuroyanagi et al. (Ref 21), only single-crystalline particles allow for the accurate determination of mechanical properties, making them preferable in AD modeling. Therefore, despite the typical use of polycrystalline powders with large grain sizes, the simplification to single-crystalline particles is reasonable for the objectives of this research, particularly given their relevance in accurately modeling mechanical properties.

The impact models consisted of single-crystalline particles in sizes of 10, 25, 35, 50, 200 and 300 nm, as well as single-crystalline rigid substrates with lengths of 1.5 times the particle diameters. This substrate length was selected to reduce computation time. The rigid substrate behavior was selected to avoid any influence by substrate deformation on particle deceleration and thus associated stresses within the particle. This should guarantee, that only influences by binding energy, particle size and velocity determine derivable deformation features. The system size considered the expected limited flattening of brittle particles on the substrate in AD. Substrates and particles are assumed to have the same atomic structure and orientation (epitaxy). Figure 1(b) shows the model setup for MD particle impact simulation. Substrates were assumed to be rigid in order to keep the same boundary conditions under variations of velocity or particle strength, thus avoiding influences by substrate deformation onto deceleration during the impact.

Before impact simulations, the nanoparticles were initially equilibrated at room temperature (300 K) for several pico-seconds (ps). The particles were then shot onto the substrates under an angle of 90°. The impact velocities varied in a range from 100 to 1100 m/s. The particle impact scenarios were studied for velocity intervals of 50 and 100 m/s. No periodic boundary conditions were applied on the substrate or the simulation box. As for the tensile tests, the Velocity Verlet algorithm (Ref 17) was employed in particle impact simulations to integrate the equations of motion with time steps of 5×10^{-15} s.

The atomic shear strain analysis was performed using OVITO software (Ref 19) to study the particle impact behavior and attain deformation patterns. The maximum atomic shear strain, i.e., τ_{max} , in 2D is calculated from three components of the atomic strain tensor as per Eq. 4. The

maximum atomic strain in Eq. 4 is calculated by the relative displacement of neighboring atoms and a defined cut-off radius, which is different from the cut-off distance in the M-LJ potential and determines the number of the neighbor atoms for calculation of the strain tensor (Ref 22).

$$\tau_{max} = \sqrt{\left(e_{XY}^2 + \frac{(e_X - e_Y)^2}{2} \right)} \tag{Eq 4}$$

Temperature Calculation

For the selected particle impact conditions, temperatures were calculated for both whole particles and local areas inside the particles using Eq. 5. In this equation, the temperature of a group of atoms is determined based on their kinetic energy, with the translational and angular velocities of the center-of-mass of the atom group subtracted. This step is essential to eliminate any overall translational and angular motion of the entire system, directing attention to the internal motions of the atoms (Ref 17). In this equation, $dim = 2$ is the dimensionality of the 2D-MD simulation, N_{atoms} is the number of atoms in the group of atoms, k_B is the Boltzmann constant, T is the absolute temperature, m is the atomic mass and v_X , v_Y and v_{XY} refer to the atomic velocities in X , Y and XY axes, after subtracting the velocity of the center of mass of the particles. In molecular dynamics simulations, the initial velocities of atoms are often set randomly based on the Maxwell–Boltzmann distribution. The initially assigned velocities are then adjusted or scaled so that the system achieves a specific temperature, often room temperature.

$$\frac{dim}{2} N_{atoms} k_B T = \frac{1}{2} \sum_{i=1}^{N_{atoms}} m(i) (v_X^2(i) + v_Y^2(i) + v_{XY}^2(i)) \tag{Eq 5}$$

When calculating the overall mean particle temperature, the summation of kinetic energy in Eq. 5 includes all atoms of one particle at a given time. In the case of local temperatures, however, the summations pertain to an ensemble of a few tens of atoms located in a gridded domain by chunks. In this study, a single chunk is a spatial bin that includes 20 atoms. The simulation box in this study is gridded by chunks at every several timesteps in order to map each atom into a 2D chunk based on its current position in the X and Y axes. Subsequently, the local temperature is calculated from the kinetic energy of atoms in each chunk as per Eq. 5. In this study, the particle’s mean temperatures and the local temperature are calculated by LAMMPS (<https://lammps.sandia.gov>), and the local temperature fields are plotted by using OVITO version 3.0.0 (www.ovito.org) (Ref 19).

Atomic Misorientation Calculation

The recognition of the grain refinement in 2D was carried out by analysis of the atomic rotation tensors (Ref 10, 19). The atomic rotation tensors are obtained by polar decomposing the atomic deformation gradient into (i) the atomic rotation tensors (Θ_z) and (ii) the stretch tensors using OVITO. The deformation gradient is calculated based on two input atomic configurations using OVITO: (i) the reference configuration and (ii) the current (or deformed) configuration (Ref 19). The reference configuration is the initial arrangement of atoms inside the particle and substrate from frame 0. Despite the limitation of using frame 0 as the reference, which prevents highlighting misorientation between the particle and substrate at that frame, it remains a valuable approach for emphasizing atomic misorientation or grain refinement in this study.

The investigation into grain refinement is confined to two particle sizes, namely, 50 and 300 nm. Preliminary simulations revealed that at smaller scales, the crystallographic orientation mismatch between the 50 nm particles and the substrate markedly affects grain refinement. Consequently, a deliberate adjustment is made by 30° tilting the 50 nm particles before they collide with the substrate. On the other hand, for the 300 nm particles, no pre-tilting is necessary to thoroughly study the details of grain refinement.

Results

Simulated Stress–Strain Dependence Under Quasi-Static Loads

The influence of the binding energies on the mechanical properties of the M-LJ potential materials was investigated

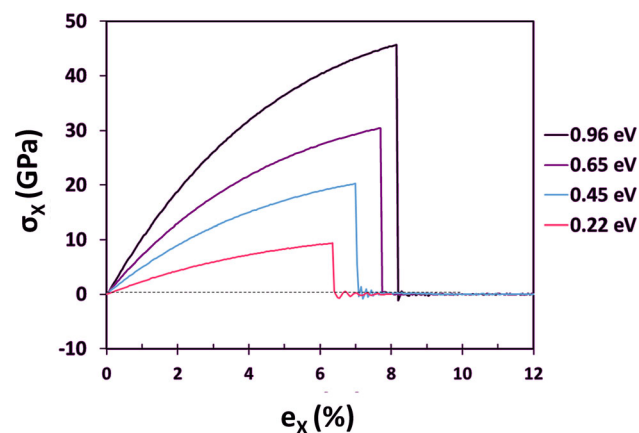


Fig. 2 Simulated stress–strain curves of brittle materials with different binding energies. The deformation in the X-axis was applied by a displacement rate of 0.1 m/s (Ref 23)

by their respective tensile stress–strain curves, as given in Fig. 2. The stress–strain curves reveal that the slopes representing YOUNG’s moduli as well as the maximum attainable stresses increase with rising binding energies. The observed maximum stresses at yield/fracture point of the M-LJ materials are attributed to their defect-free single-crystal structures, here nearly reaching the theoretical strengths. The stress–strain correlations given in Fig. 2 deviate from the typical linear behavior with the elastic regime of brittle bulk materials. This nonlinearity is attributed to the decreasing rate of increase in interatomic forces with atomic distances at the atomic scale. As described by Eqs. (2) and (3), the stress is determined by two components: (a) the kinetic energy, which is negligible at room temperature, and (b) the virial pressure contribution. The latter is derived from interatomic forces (or pairwise interactions) and interatomic distances (r_i), as specified by Eq. 3. Within Lennard–Jones systems, the pairwise interactions vary due to changes in interatomic distances. This results in a nonlinear behavior, as given by the stress–strain curves in Fig. 2. From Fig. 2, YOUNG’s moduli were determined by calculating the slope of a line drawn between $e_x = 0$ and e_x at the point of maximum attainable stress.

In Fig. 3a, the M-LJ potentials are plotted versus the interatomic distance between two atoms over a wide range of binding energy values. The interatomic force diagram in Fig. 3b was then plotted by deriving the M-LJ potentials with respect to the interatomic distance. Figure 3b depicts that M-LJ materials possessing higher binding energy show larger attractive atomic forces. Consequently, M-LJ materials with higher binding energies require larger stress levels to overcome interatomic forces to initiate fracture (maximum values in the curves of Fig. 2). This also leads to a higher fracture strain for the M-LJ material with larger binding energy. The slopes of the correlation between interatomic force and atomic distance decrease (Fig. 3b), which might have consequences for the stress–strain behavior under external tensile loads.

Snapshots taken from the tensile test model at the end of the respective simulations after fracturing are provided in Fig. 4. All samples show fracture mainly occurring orthogonal to the applied stress direction, thus indicating brittle fracture (similar to the fracture mode I). Table 1 summarizes the key data from tensile test simulations. Deriving YOUNG’s moduli from the stress–strain curves allows for a comparison to real materials based on tabulated mechanical property data. Examples of respective ceramic materials are also included in Table 1.

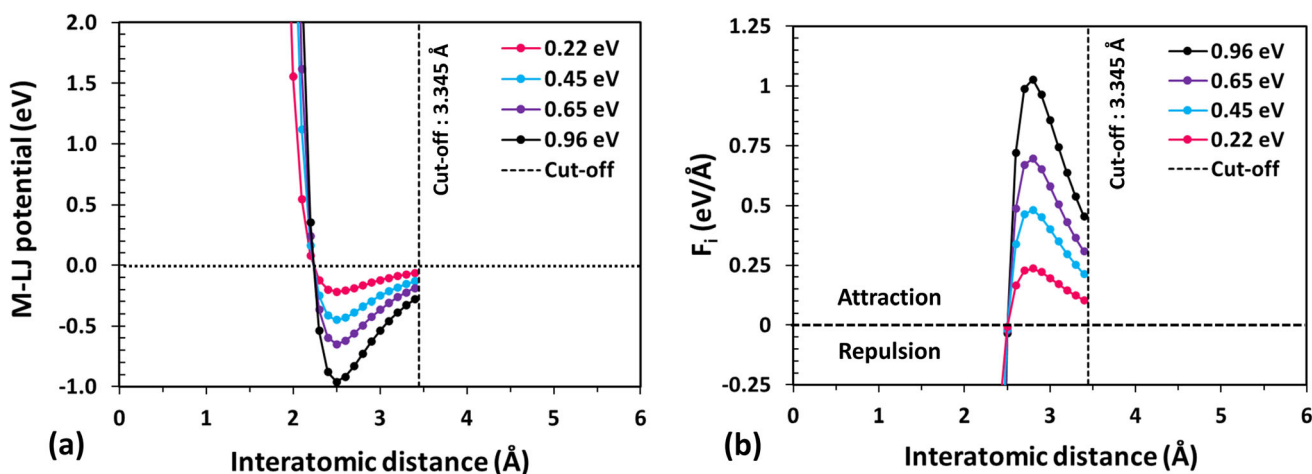


Fig. 3 Plots of the M-LJ potentials and the resulting atomic force (F_i) diagrams against interatomic distance are presented for four different binding energies, ranging from 0.22 to 0.96 eV, in (a) and (b), respectively. The selected cut-off distance in the M-LJ potentials is

considered to be $1.5 \times \sigma = 3.345 \text{ \AA}$. The equilibrium interatomic distance between each pair of atoms is 2.5 Å. The plots indicate that interatomic forces are nonlinear

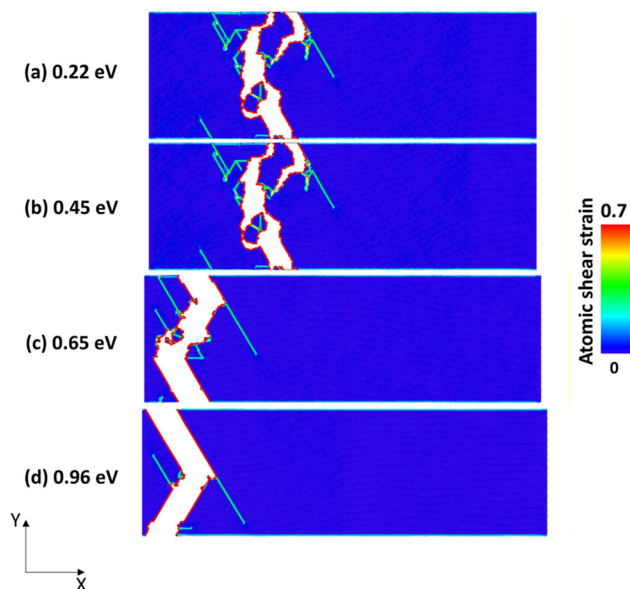


Fig. 4 Snapshots of atomic shear strain fields resulted from tensile test MD simulations for materials with different binding energies. Plots show a very small amount of plastic deformation (green fields) before brittle fracture in each model

Particle Impact Simulations—Deformation Pattern and Fracture

As introduced in the tensile test simulation part, particle impact scenarios were modeled for a set of four different binding energies and wide ranges of particle sizes and initial velocities. In the following, details of impact morphologies are only given for typical examples to illustrate differences in deformation behavior. For these graphs, rather different particle sizes of 50 nm (Fig. 5) and 300 nm (Fig. 6) are selected in order to distinguish the main

influences of different binding energies on possible bonding or fragmentation features. However, the whole data set is then used to derive more general aspects and trends.

Particle velocities of 200, 400 and 600 m/s were selected to illustrate different impact scenarios. This velocity range corresponds to real conditions in AD and allows covering possible bonding phenomena given for the different binding energies. Such has been validated by individual MD simulations and estimated threshold velocities for bonding by using a theoretical approach (Ref 10). Respective data are given in Table 2. As shown from Fig. 5 and 6, it is reasonable to use the contrasts within the shear strain field of the particles to deduce information on deformation patterns and reasons for possible fragmentation. In view of interpreting the associated deformation mechanism in terms of shear strain fields, it must be explained that—according to the formal definition of Burger’s vector—one step of sliding atomic planes in a 2D closed-packed structure should result in a value of $\vec{b} = 2 \tan(\pi/6) = 1.15$ (unitless). Such displacement between two adjacent atomic configurations leads to a shear strain value of 0.58. Thus, the color codes from green to red in the shear strain fields of Fig. 5 and 6 correspond to a displacement equal to or greater one Burger’s vector and thus plastic deformation within the particles. That allows using the shear strain fields to distinguish locally occurring plastic deformation for particles with different binding energies at different velocity regimes.

Figure 5 gives an overview of attainable impact morphologies for a particle size of 50 nm. The given times of 20–30 ps after the first particle contact with the substrate corresponds to situations that allow distinguishing the main deformation features. The first line of Fig. 5 summarizes

Table 1 The (i) maximum strength, (ii) strain to failure and (iii) YOUNG's modulus according to results from the tensile test simulations for materials with different binding energies, in comparison with real material data

Artificial ceramics				Similar real ceramic*	
Binding energy, eV	Maximum strength, GPa	Failure strain, %	YOUNG's modulus, GPa	Material	YOUNG's modulus, GPa
0.22	9.39	6.35	148	Silicon	62-180
0.45	20.26	7.00	289	Anatase TiO ₂	230-288
0.65	30.00	7.80	384	Alpha-alumina	370-460
0.96	45.70	8.14	561	Tungsten carbide	530-700

*Taken from www.matweb.com, accessed at 05.21.2023, 15:05 a.m.

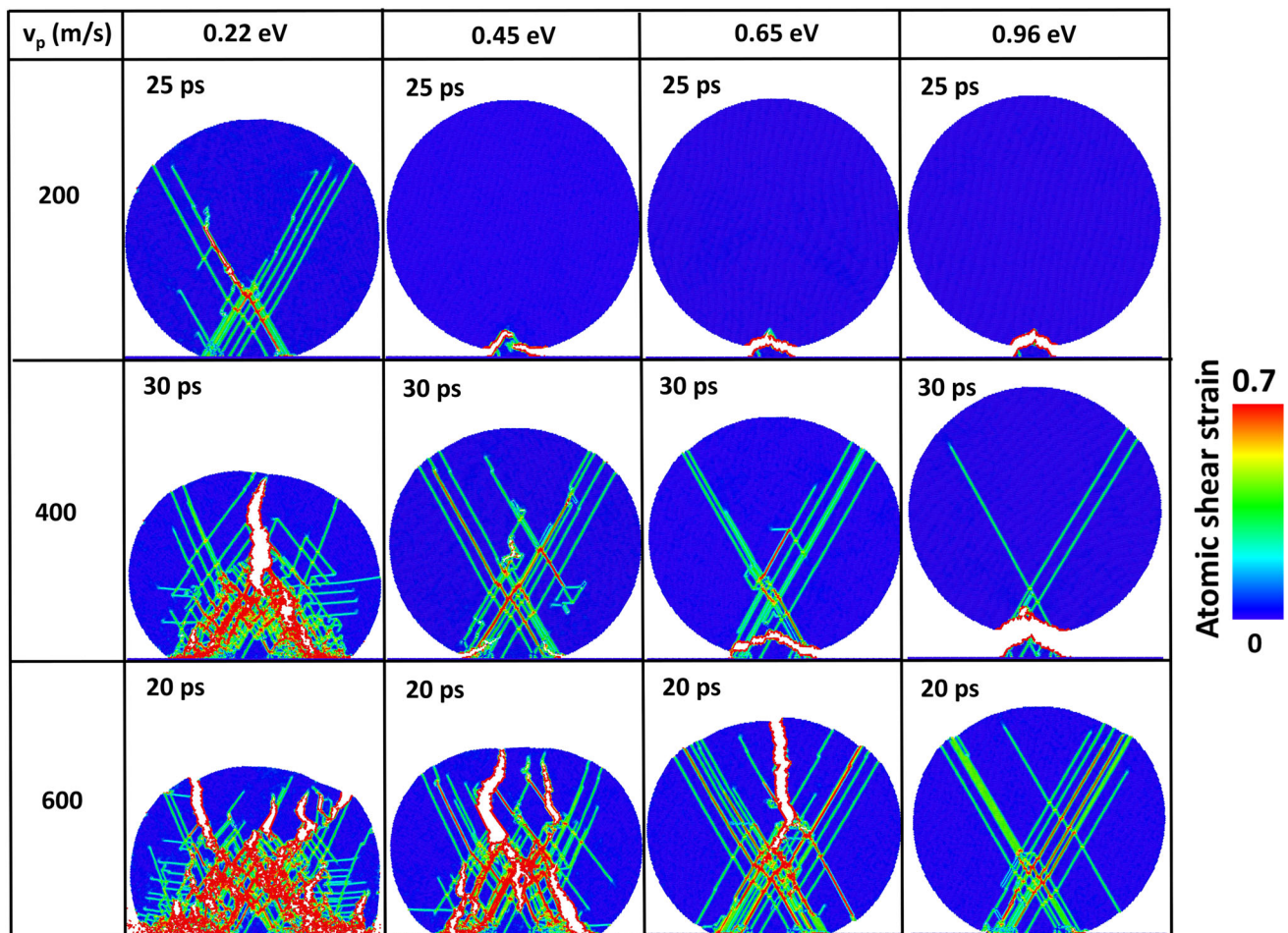


Fig. 5 Impact morphologies and associated shear strain fields of 50 nm particles as simulated with different binding energies and different impact velocities. The snapshots were taken 25 ps after the

collision at 200 m/s, 30 ps after the collision at 400 m/s and 20 ps after the collision at 600 m/s

the attainable features for an impact velocity of 200 m/s at 25 ps after the collision of the particles to the substrates. The time of 25 ps is already sufficient to show the final impact deformation and fracture pattern of the 50 nm particles with different binding energies. At a velocity of 200 m/s, the 50 nm particle with a binding energy of 0.22 eV shows bonding to the substrate surface. The

particle is slightly flattened and shows internal deformation features by stain contrast. The strain fields spread from the contact zone to the substrate into the particle interior. In contrast, particles with binding energies of 0.45, 0.65 and 0.96 eV rebound at a velocity of 200 m/s, leaving some traces of deformed material at the substrate. In the case of rebounding, the reached distances to the substrate scale

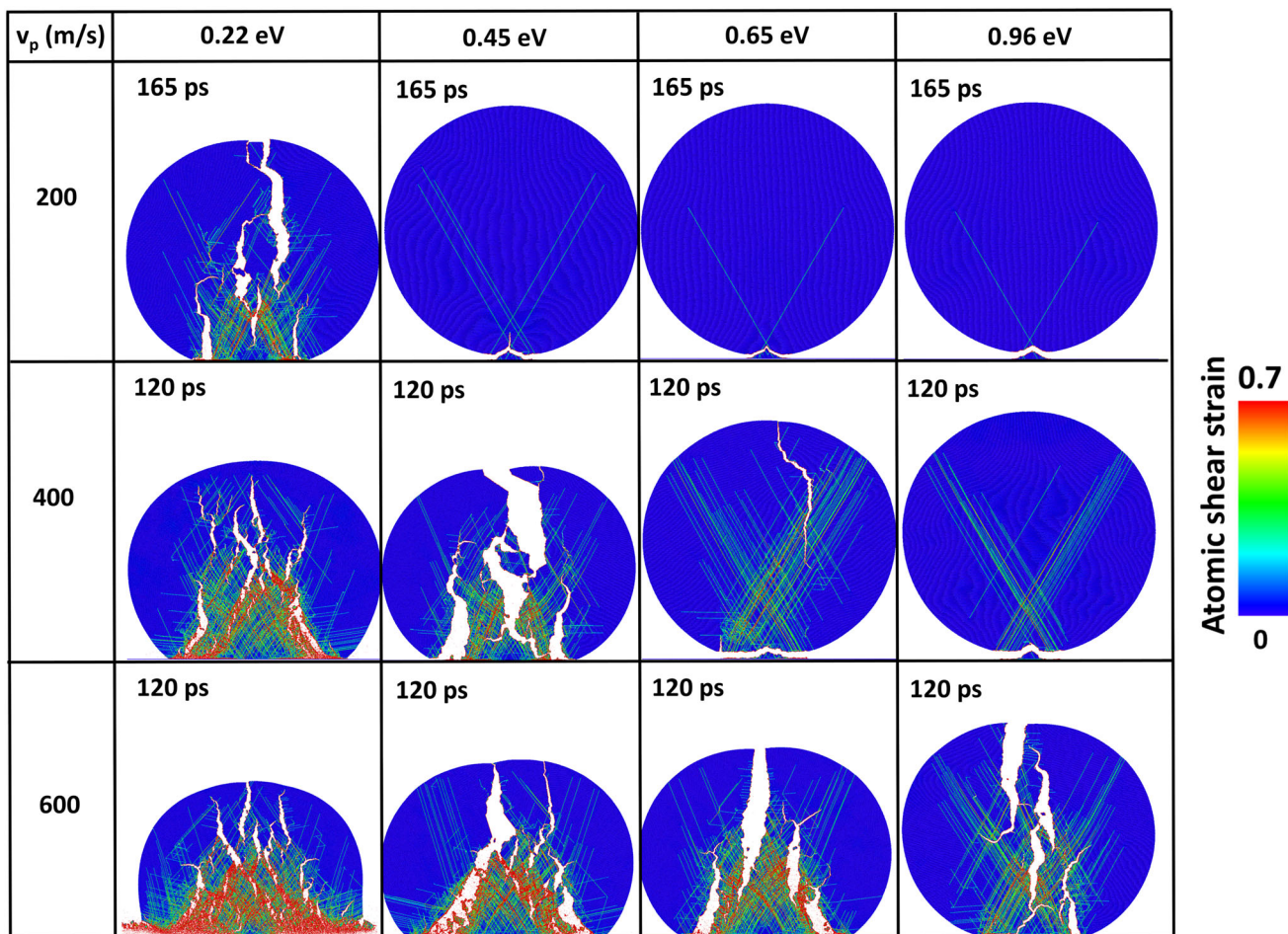


Fig. 6 Deformation pattern and associated shear strain fields of 300 nm particles as simulated for different energies and different impact velocities. The snapshots were taken 165 ps after the collision at 200 m/s and 120 ps after the collision at 400 and 600 m/s

Table 2 Required threshold velocities for bonding as calculated from the analytical approach (10) compared to validated MD results

Binding energy, eV	YOUNG’s modulus, GPa	v_{thre} , m/s	
		Analytical	MD results
0.22	148	270	200
0.45	289	378	400
0.65	384	436	500
0.96	561	527	600

with binding energies. This indicates that higher binding energies result in shorter times to initiate fracture within that bottom particle part close to the substrate.

At 400 m/s, the MD snapshots were taken 30 ps after impact. This time was selected to illustrate the fracture of the 50 nm particle with a binding energy of 0.22 eV just before separating to the fragmented pieces. The strain contrast reveals pronounced internal particle deformation with the highest concentration along a triangle spreading from the interface to the substrate into the particle center. At this velocity, the particle with the binding energy of

0.45 eV bonded to the substrate without fracture. In contrast, the particles with the binding energies of 0.65 and 0.96 eV rebounded despite already occurring internal strain fields. The observed amounts of inelastic deformation decrease with increasing binding energies and are not sufficient to compensate for elastic rebound forces. At a fixed time of 30 ps, distances to the substrate are larger in the case of the higher binding energy of 0.96 eV than for the particle with a binding energy of 0.65 eV. Consequently, it can be assumed that separation from the substrate occurs earlier for higher binding energies.

At 600 m/s, the 50 nm particles with binding energies of 0.22 and 0.45 eV fractured into several parts 20 ps after the collision. Thus, MD snapshots were taken after 20 ps, just before the separation of the fragmented pieces under ongoing deformation (for the sake of space not shown in this paper). In contrast, the 50 nm particle with the binding energy of 0.65 eV bonded to the substrate but shows a meridional crack at the top. However, the crack did not grow further after this time step, nor did the particle separate from the substrate (not shown in this paper). At 600 m/s, the 50 nm particle with the binding energy of 0.96 eV bonded to the substrate without cracks. Within the MD simulations, the particle with a binding energy of 0.96 eV started to show fragmentation at a velocity of 850 m/s, which is not included in this figure.

According to Fig. 5, the major features under impact of a 50 nm particle could be summarized as follows. The amount of plastic deformation and, thus, particle flattening increase with increasing velocity and decreasing binding energies. Occurring strain mainly concentrates on the bottom part of particles and stretches from the interface to the substrate into the particle center, resulting in a triangular shear zone. Attained strains are highest at intersections of deformation regimes and close to fracture zones. Bonding of whole particles (compare; 0.22 eV, 200 m/s; 0.45 eV, 400 m/s; 0.65 eV, 600 m/s and 0.96 eV, 600 m/s) is associated with more prominent plastic deformation spreading as a triangle-shaped region from particle/substrate interface toward particle center. On the other hand, the fractured particles, i.e., (0.22 eV, 400 m/s), (0.22 eV, 600 m/s) and (0.45 eV, 600 m/s) reveal that fragmentation is associated with (i) meridional cracks (Ref 8, 10) and (ii) shear cracks (Ref 10). The meridional cracks are mainly perpendicular to the substrate interface, parallel to the impact direction and grow from the upper part of the particle (Ref 8, 10). The meridional cracks can also be observed in bonded particles (0.65 eV, 600 m/s). The shear cracks appear at higher impact velocities around the triangle-shaped regions where the shear strain becomes too high. The formation of shear cracks, which enclose the triangle-shaped region, is more prominent for lower binding energy, i.e., 0.22 and 0.45 eV.

This result motivated a detailed study of the features under identical conditions, but for a larger particle size of 300 nm. Figure 6 shows the respective results of MD impact simulations. For direct comparison to the results from Fig. 5, here as well impact velocities of 200, 400 and 600 m/s were selected to illustrate the main features of deformation and fracture. The MD snapshots of particles with different binding energies in Fig. 6 were taken at 165, 120 and 120 ps after impact. These times are sufficient to show the final shapes and accumulated deformation within the particles.

At 200 m/s, the 300 nm particle with a binding energy of 0.22 eV fractured. In contrast, the particles with higher

binding energies rebounded after 165 ps. At 200 m/s, the fragmentation pattern in the 300 nm particle with the binding energy of 0.22 eV differs from those of the 50 nm particle observed in Fig. 5 at 400 and 600 m/s. The 300 nm particle mainly shows fragmentation by meridional cracks, whereas the 50 nm particle of this low binding energy failed by shear cracks. The meridional cracks are parallel to the impact direction and are caused by stresses and strains in the *X*-axis (Ref 8). The general deformation features given by the strain fields are similar to those of the small particle. However, the local deformation band density is lower for the larger particle size.

At 400 m/s, the 300 nm particles with the binding energy of 0.22 and 0.45 eV fractured, while the particles with the binding energy of 0.65 and 0.96 eV rebounded. Nevertheless, different fracture patterns were observed within particles with binding energies of 0.22 and 0.45 eV. In the case of the particle with a binding energy of 0.22 eV, the velocity of 400 m/s is sufficient to cause locally high shear strain fields that, similar to the cases of smaller particles, stretch as triangle-shaped regions from the interface to the substrate toward the particle center. The high amount of deformation along this triangular shear zone could result in shear fracture, in the present case dominating over meridional fracture. In contrast, the particle with a binding energy of 0.45 eV shows less shear deformation and thus no associated cracks. The final fracture is then dominated by meridional cracks.

At 600 m/s, all 300 nm particles with the binding energy of 0.22–0.96 eV fractured, despite the significant difference in deformation. According to the shear strain pattern, the particles with lower binding energies show severe plastic deformation at the interface to the substrate and along the shear triangle zone toward the center. For higher binding energies, plastic deformation is less severe and mostly concentrated in areas of shear intersection inside the particles. It seems that higher amounts of plastic deformation in the case of lower binding energies reduce crack spreading.

For the particle size of 300 nm, the main features can be summarized as follows. Depending on velocity and binding energies, all particles either rebound or fracture. Lower binding energies and higher impact velocities promote the formation of shear strain fields and localized plasticity. Higher amounts of local shear also favor following shear fracture in competition with meridional failure. Occurring plasticity also influences the size of triangle-shaped deformation areas. If conditions for plastic deformation are reached, associated triangular shear regions form and spread wider for lower binding energies and higher impact velocities. To a certain extent, the material within these regions could withstand crack formation or crack spreading.

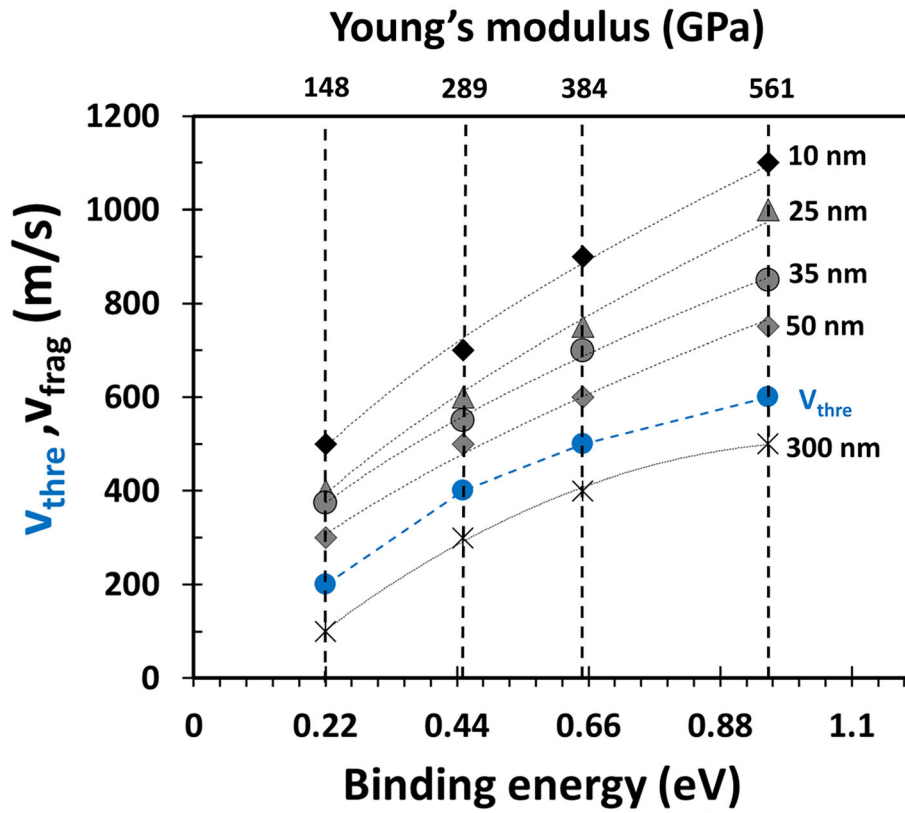


Fig. 7 Threshold and fragmentation velocities (v_{thre} and v_{frag}) as a function of particle binding energies for a range of different particle sizes

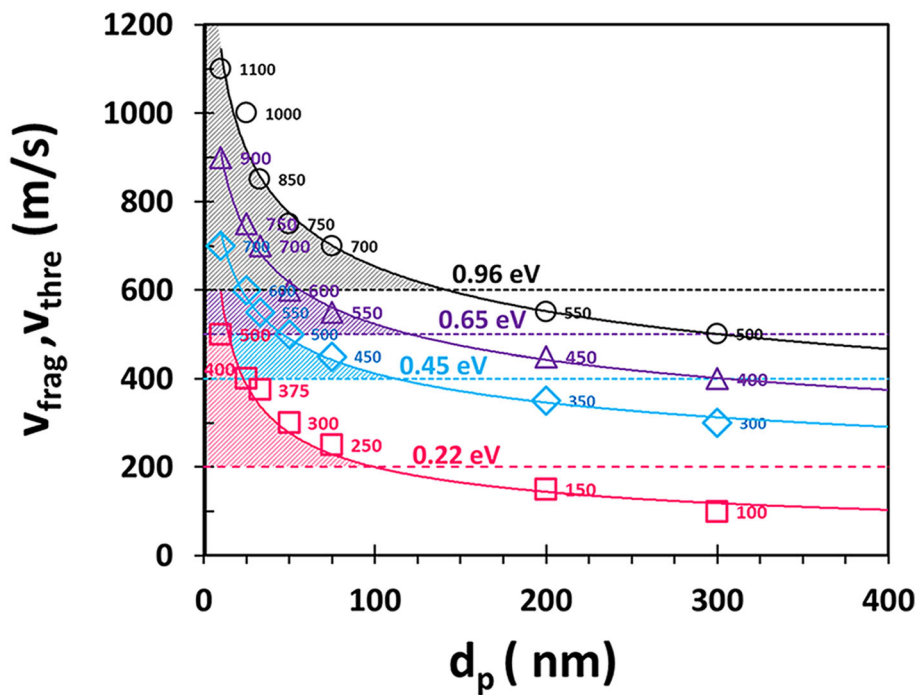


Fig. 8 Ranges of threshold (dotted lines) and fragmentation velocities (open symbols) of particles with different binding energies plotted against particle sizes. The hashed regions with the same color

as the threshold velocity lines indicate the individual windows of deposition for each binding energy

Particle Impact Simulations—Threshold and Fragmentation Velocities

The results from subsequent, previously introduced MD simulations allow for distinguishing the main features under particle impact and allow extracting information on transition regimes with respect to the investigated parameter combinations of impact velocities, binding energies and particle sizes. The threshold velocity v_{thre} defines the transition between rebounding and bonding of whole particles, whereas the fragmentation velocity v_{frag} describes conditions that lead to crack formation. Both depend on locally predominant deformation conditions and overall stress states.

The threshold and fragmentation velocities, i.e., v_{thre} and v_{frag} , resulting from the conducted MD simulations for the investigated particle diameters and binding energies are given in Fig. 7. This figure also provides the YOUNG's modulus associated with the respective binding energies according to Fig. 2 and Table 1. The results show that threshold velocities increase with binding energies. However, in agreement with the literature (Ref 10), the threshold velocities do not vary with particle size. Therefore, this plot only shows one common threshold velocity for the different particle sizes.

The fragmentation velocity increases with increasing binding energy but decreases with increasing particle size. Bigger particles are more prone to fracture. Thus, for constant binding energy and within the given range of particle sizes from 10 to 300 nm, the fragmentation velocities decrease by about 2–5 times, and the slopes of fragmentation velocities here slightly decrease with increasing binding energy. Furthermore, it seems that both threshold and fragmentation velocities vary similarly with the binding energy parameter. In the case of a particle size

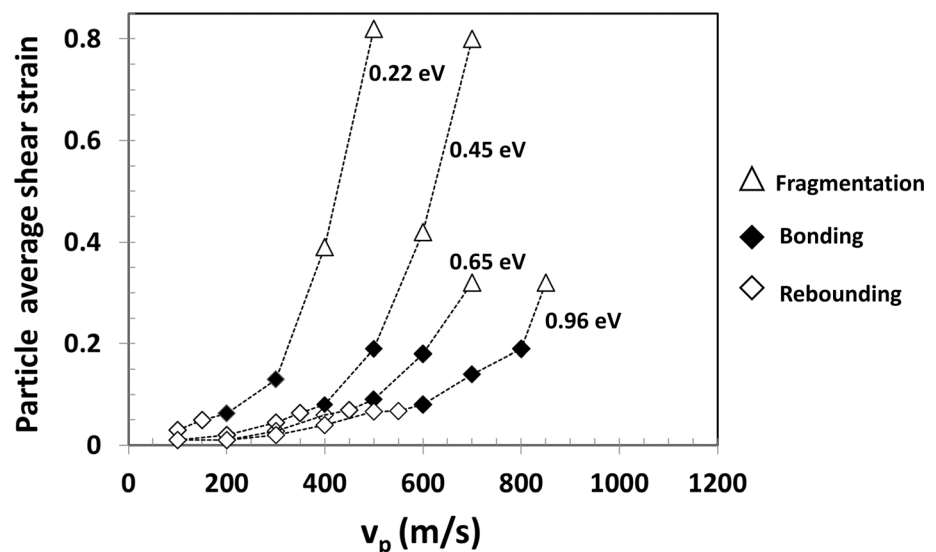
of 300 nm, for all investigated binding energies, the fragmentation velocities even become smaller than the threshold velocities, with the time for meridional fracture being shorter than the time for separation. An example is given in the MD snapshot of the 0.65 eV particle at 400 m/s in Fig. 6, showing the formation of a meridional crack inside a rebounded particle.

In order to extract ranges of whole particle deposition, here defined as bonding, for the different binding energies in accordance with the previous studies (Ref 7–10), the data shown in Fig. 7 are arranged in a different manner within Fig. 8. Herein, the particle threshold and fragmentation velocities are plotted against the particle diameters. The range of whole particle bonding is limited by the threshold and the fragmentation velocities, here given by straight dotted lines and open points, respectively. The derived windows of deposition are indicated by the hashed regions in Fig. 8. The regimes for bonding stretch over similar areas for all binding energies. However, the deposition fields rise to higher velocities with increasing binding energies. Higher binding energies, on the other hand, allow to avoid fracture for slightly increased particle sizes. Assuming that fracture of bonded particles is unavoidable under secondary impacts, exceeding the threshold velocity could be taken as the main measure for layer formation. This means that materials with lower binding energies have a smaller threshold velocity, allowing for easier coating formation by using AD compared to materials with higher binding energies.

Particle Impact Simulations—Consequences of Local Plasticity for 50 nm Particles

The deformation morphologies and trends with respect to binding energies and particle sizes, presented in previous

Fig. 9 Average atomic shear strain for 50 nm particles plotted against the impact velocity. The average shear strain was calculated when the bonded particles (dark-filled diamonds) reached the equilibrium state on the substrate. However, calculations were carried out for the rebounded particles (non-filled diamonds) just after rebounding and before moving far from the substrate. In the fragmented particles (triangles), calculations were performed just before separating the deformed particles into fragmented pieces



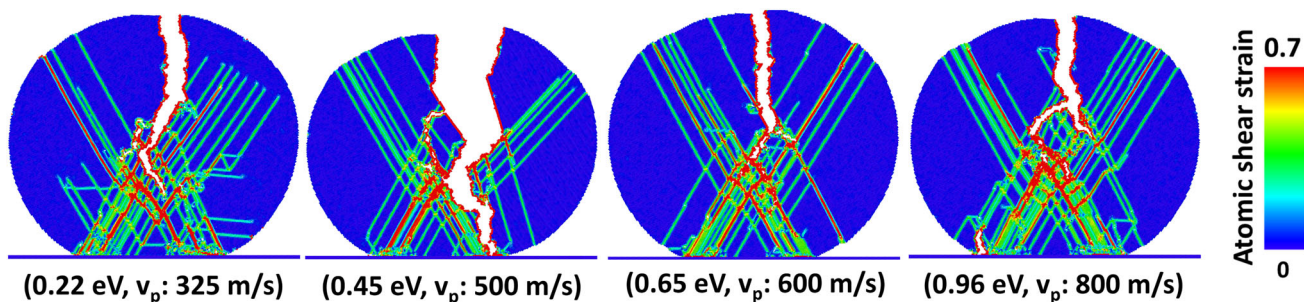


Fig. 10 Particle deformation in terms of shear strain and fragmentation pattern for different binding energies at impact velocities that cause the average atomic shear strains of about 0.2 in particles of

50 nm size. The individual velocities were chosen based on the intersections of a straight line, corresponding to the particle’s average shear strain of 0.2, with the curves illustrated in Fig. 9

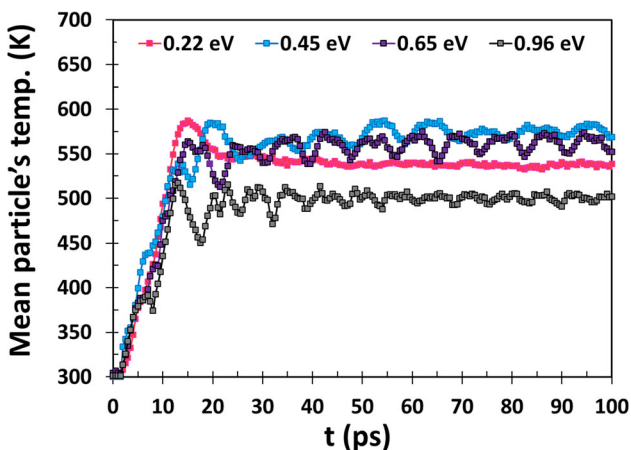


Fig. 11 Calculated mean particle temperature using Eq. 5 for 50 nm particles of different binding energies that impact the substrate with a velocity of 400 m/s from the impact time when the particle hits the substrate

sections, demonstrate that the observed features for deformation and possible layer formation are similar and mainly governed by impact velocity. Differences with respect to fracture are mainly attributed to size-dependent crack formation and growth, as will be seen in this section. Thus, features occurring within the mainly plastic deformation regimes could be taken as a measure for deriving differences caused by binding energies, independent of individual particle sizes. Some of the general trends that could be important for the understanding of AD are presented below.

For a particle of 50 nm diameter, Fig. 9 depicts the role of binding energies on the particle’s average shear strain. Herein, the average shear strain was obtained by averaging the shear strain over all the atoms in the particle once the bonded particles reached the equilibrium state on the substrate. For this purpose, the atomic shear strain data were first calculated using OVITO and then averaged over the whole atoms for each particle. In this diagram, the particle’s average shear strain is plotted against impact velocities for each investigated binding energy. The different

impact behaviors of the particles are distinguished by symbol types. Triangles indicate fragmented particles, dark-filled diamonds bonded particles and non-filled diamonds the rebounded particles. The slopes of the different curves indicate that average shear strain decreases with increasing binding energy. Particles with lower binding energies appear as prone to deformation and shearing than those with higher binding energies. Furthermore, this plot shows that fragmentation occurs inside the particles for an average shear strain of approximately 0.2. The authors expect that the average shear strain necessary for fragmentation increases with increasing binding energy. However, the type of correlation is yet an open question. The actual fragmentation criteria need to be clarified in the future investigations.

Figure 10 shows the impact behavior of 50 nm particles for combinations of different binding energies and impact velocities that cause an average atomic shear strain of approximately 0.2 within the particles. The snapshots in Fig. 10 were taken after the particles had reached equilibrium, except for the case of a binding energy of 0.45 eV and respective parameter sets where fragmentation separated the particle. The snapshots show fragmented particles, all showing a large meridional crack growing from the top of the particles. Within the limits of this rough analysis, this confirms that the fragmentation behavior of 50 nm particles is reached at an average shear strain of approximately 0.2.

Temperature Analysis

Particle bonding in AD could be also influenced by local temperature. Possible effects of released heat by plastic deformation during particle impact and associated local temperature rises were investigated and described in the following. Since results are presented in Fig. 5 and 6 for particles with diameters of 50 and 300 nm, respectively, the subsequent discussion is restricted to these particle sizes too.

As an example, Fig. 11 provides the mean temperature of 50 nm particles of different binding energies for the same impact velocity of 400 m/s. In the case of a particle with a binding energy of 0.22 eV, the mean temperature first rises to 585 K before stabilizing at an equilibrium temperature of around 535 K at 80 ps. However, from the snapshots presented in Fig. 5, it is evident that this particle fragments. As derived from the full impact sequence (not shown here), the particle starts to fracture 20 ps after the collision time, and three segments are formed and separated after 25.5 ps, the centrally located, deformed triangular area remains on the substrate, and the other two parts drift in opposite directions to the sides. Thus, the calculated mean temperature represented here by the pink curve accounts for the whole particle temperature only up to 25.5 ps after the collision time (the peak up to about 590 °C in the pink curve). From 25.5 to 100 ps, the calculations then consider the temperatures of the fragmented pieces too, and therefore, the calculated particle

temperature is not reliable. In the time interval from 25.5 to 100 ps, the overall particle temperature then decreases to 535 °C.

In the particle with the binding energy of 0.45 eV, the mean particle's temperature rises to 585 K after about 20 ps and then fluctuates. The observed temperature fluctuations after reaching equilibrium are an inherent issue in MD simulations, primarily due to statistical effects arising from the finite particle sizes. This effect is more pronounced in smaller systems in MD and diminishes in larger ones.

In a particle with a binding energy of 0.65 eV, the mean particle's temperature rises due to the plastic deformation to 560 K at 15.5 ps just before the start of the rebounding behavior. The observed temperature fluctuations after 15.5 ps are as well due to MD modelling features according to finite particle size. In a particle with a binding energy of 0.96 eV, the mean particle's temperature rises to only 517 K at 13 ps just before the start of the rebounding behavior and then decreases to around 500 K—similar to

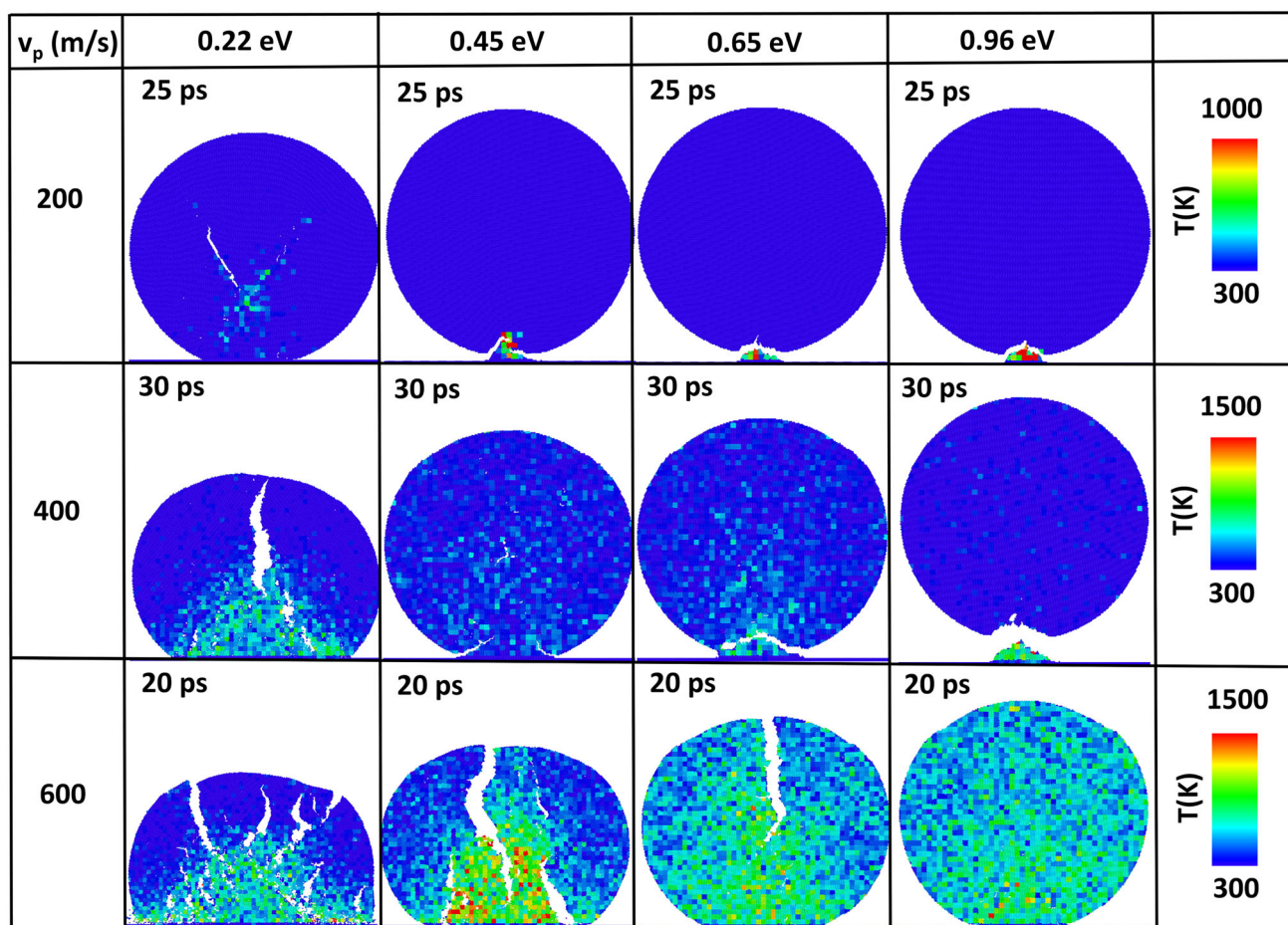


Fig. 12 Simulated impact morphologies and associated local temperature fields of 50 nm particles with different binding energies (0.22, 0.45, 0.65 and 0.96 eV) at impact velocities of 200, 400 and 600 m/s, respectively. In accordance with Fig. 5, the snapshots were

taken 25 ps after the collision at 200 m/s, 30 ps after the collision at 400 m/s and 20 ps after the collision at 600 m/s. Please note the different temperature scale bars for v_p equal to 200 m/s

the trend observed in the rebounded particle with a binding energy of 0.65 eV. The comparison between overall particle temperatures and individual deformation and fracture modes reveals that heat generation and temperature rises are attributed to plastic deformation. As long as fragmentation does not play a dominant role, most of the initial kinetic energy is transferred into elastic and plastic deformation. Higher binding energies lead to more elastic deformation and rebound kinetic energy. However, the amount of energy converted to heat by plastic deformation scales with the binding energy. Thus, average temperatures rise to a comparable level for all binding energies here. Nevertheless, considering the distinct localization of shear deformation, the average is somewhat misleading, and it can be assumed that the local temperature in the area of high shear deformation is still much higher.

Therefore, in addition to the global overall temperature rise by shear deformation, local temperature distributions could reveal more details on heat release and prospective influences by binding energies. Evaluations of local

temperature distributions were then performed for 50 and 300 nm particles based on their local shear strain fields as a measure of plastic deformation given in Fig. 5 and 6. Earlier researches (Ref 8, 10) have highlighted that the local temperature within fragmented particles rises significantly within the sections that remain on the substrate, but only dealt with a binding energy of 0.45 eV.

Figure 12 shows the local temperature distributions inside the 50 nm particles for different binding energies and impact velocities according to the selection of snapshots of the deformation pattern in Fig. 5. At 200 m/s, in the 50 nm particle with the binding energy of 0.22 eV, local temperature fields reach a maximum temperature of around 450 K. The comparison of local temperature fields (Fig. 12) with that of the strain distribution fields (Fig. 5) in the particle with the binding energy of 0.22 eV shows that local heat generation is associated with plastic deformation inside the particle. At the same velocity, the local temperatures of rebounded particles with binding energies of 0.45, 0.65 and 0.96 eV remain at 300 K by missing internal

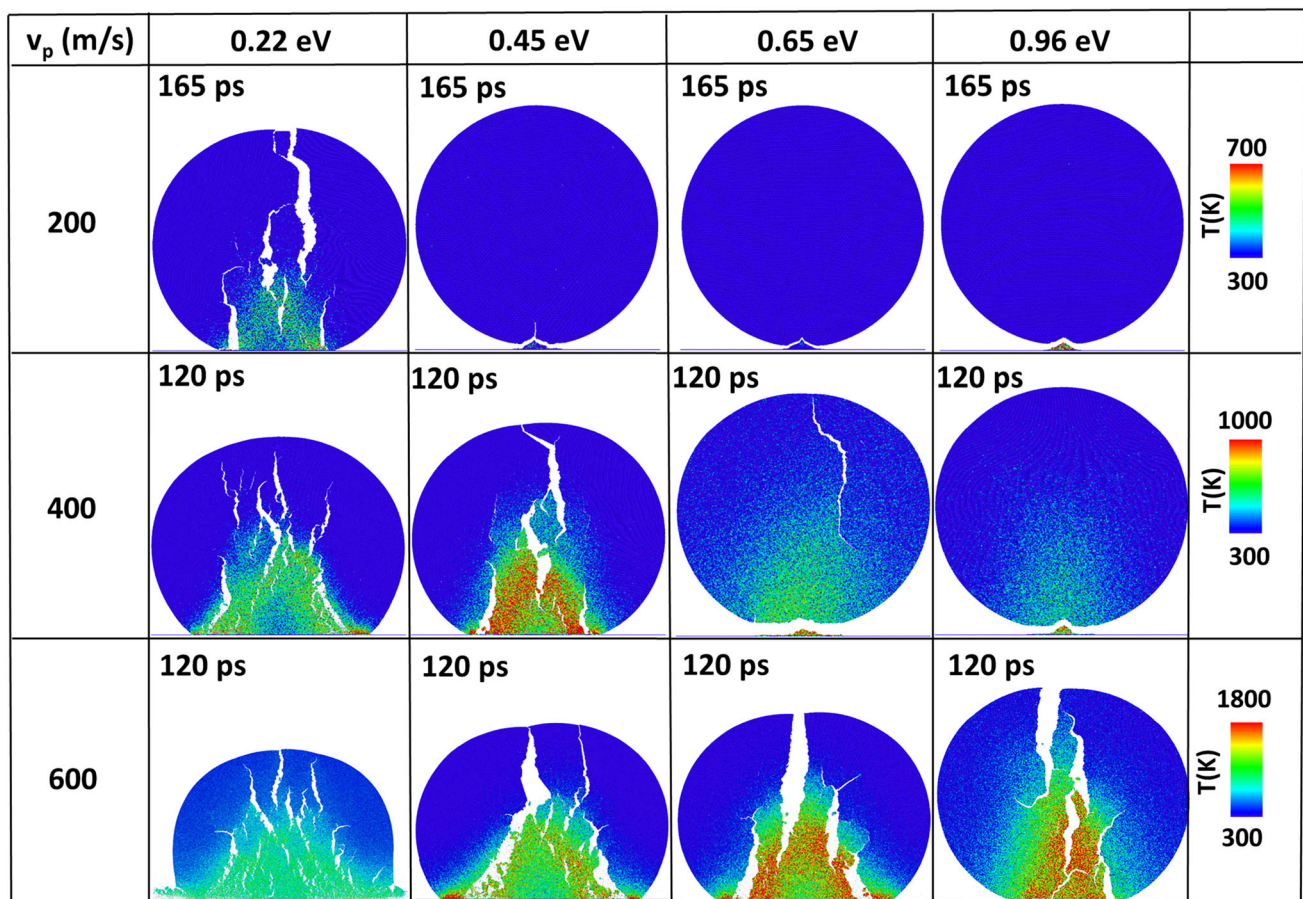


Fig. 13 Simulated impact morphologies and associated local temperature fields of 300 nm particles with different binding energies (0.22, 0.45, 0.65 and 0.96 eV) at impact velocities of 200, 400 and 600 m/s, respectively. In accordance with Fig. 6, the snapshots were

taken 165 ps after the collision at 200 m/s and 120 ps after the collision at 400 m/s and 600 m/s. Please note the different temperature scale bars for each impact velocity

plastic deformation. However, for these cases, the local temperatures within the small and plastically deformed remnants on the substrate could reach up to about 1000 K.

After 30 ps from the collision at 400 m/s in the fragmented particle with a binding energy of 0.22 eV, the local temperature within the plastically deformed areas increases to about 950 K. After 30 ps from the collision at 400 m/s, temperature fields in the particle with the binding energy of 0.45 eV are locally spread and could be attributed to previous deformation. The observed uniform temperature distribution might be attributed to heat diffusion after initial deformation. After 30 ps from the collision at 400 m/s, the rebounded particle with a binding energy 0.65 eV shows a uniform increase within local temperature distributions. This could be attributed to the plastic deformation before the rebound. At the same time and velocity, the rebounded particle with a binding energy of 0.96 eV shows only a minor internal temperature increase, which is attributed to the lack of plastic deformation. However, the left remnants on the substrate show a rather homogeneous temperature of about 700 K, the local distribution is due to plastic deformation and following heat diffusion.

Rises in local temperature distribution are also seen at 600 m/s in particles with binding energies of 0.22 and 0.45 eV, with local temperatures reaching a maximum of 1150 and 1350 K, respectively. Despite the lower amount of overall plastic deformation, local temperatures are higher for the particles with higher binding energy. For both cases, internal cracks could block further heat diffusion. In the particle with a binding energy of 0.65 eV, where only a meridional crack is created at the top of the particle, compared with its counterpart in Fig. 5, the temperature fields show a gradient from the bottom to top, with the highest of about 1150 K within the more prominently deformed shear triangle. Similar features are observed in the 50 nm particle with the binding energy of 0.96 eV that bonded at 600 m/s. Maximum temperatures reach about 1150 K. For all cases, the smooth gradients in temperature distribution indicate local heat generation is followed by heat diffusion, making the process less adiabatic at these small length scales. Nevertheless, local temperatures could increase to more than 1000 K in the lower part of the particles in association with deformation within the shear triangle spreading from the interface with the substrate.

The local temperature fields of the 300 nm particles with different binding energies at impact velocities of 200, 400 and 600 m/s are shown in Fig. 13 for time instances 165, 120 and 120 ps, respectively. In accordance with Fig. 6, at 200 m/s, in the fragmented particle with a binding energy of 0.22 eV, the temperature in the remaining portion of the particle at the substrate interface rose to approximately 450 K, while the temperature remained around 300 K in the other fragmented regions. On the other hand, in

particles rebounded at 200 m/s with binding energies of 0.45, 0.65 and 0.96 eV, the local temperature fields exhibit a consistent temperature of 300 K throughout all parts of the particles. This uniform temperature in all parts of the rebounded particles is attributed to the absence of plastic deformation within them at 200 m/s.

For 400 m/s and 120 ps after the collision, the fragmented particle with a binding energy of 0.22 eV experienced a temperature increase in the triangle-shaped region, reaching approximately 650 K. Meanwhile, the temperature in the other fragmented regions remained around 300 K. A similar temperature pattern is observed in the particle with a binding energy of 0.45 eV after 120 ps, where the localized temperature rose to 1000 K in the edges of the remaining triangle-shaped region on the substrate. Conversely, in particles rebounded at 400 m/s with binding energies of 0.65 and 0.96 eV, the local temperature fields display regions where the local temperature reaches 1000 K in the remaining portions of the particle on the substrate. Hence, it seems that heat adiabaticity is a common feature in the fragmented 300 nm particles. The maximum local temperature can also reach 1000 K in the triangle-shaped region.

At a velocity of 600 m/s, all 300 nm particles exhibit a fragmentation behavior characterized by a combination of shear and meridional cracks. As the binding energy increases from 0.22 to 0.96 eV, the length of the meridional cracks increases while the length of the shear cracks decreases. Consequently, an increased binding energy results in a smaller remaining portion on the substrate. The local temperature fields also indicate that the temperature can locally rise to 1800 K at the edges of the remaining portion on the substrate, particularly in particles with binding energies of 0.65 and 0.96 eV.

The results from temperature analysis can be summarized as follows: An increase in temperature is mainly constrained to areas that undergo high degrees of plastic deformation, the mean particle temperature then just depends on the overall applied plastic strain. On small length scales, heat diffusion ensures a fast spread leading to rather homogeneous temperature distributions. Locally reached maximum temperatures increase with particle velocities. In the case of fragmentation, heat diffusion is hindered then resulting in higher temperatures of originally deformed areas in the remaining portions on the substrate. The effect is more pronounced for higher binding energies, higher impact velocities and larger particle sizes.

Atomic Misorientation and Grain Refinement

This section investigates the influence of binding energy on grain refinement in particles of 50 and 300 nm, here serving as examples. Assuming a non-epitaxial impact

d_p : 50 nm, v_p : 600 m/s:

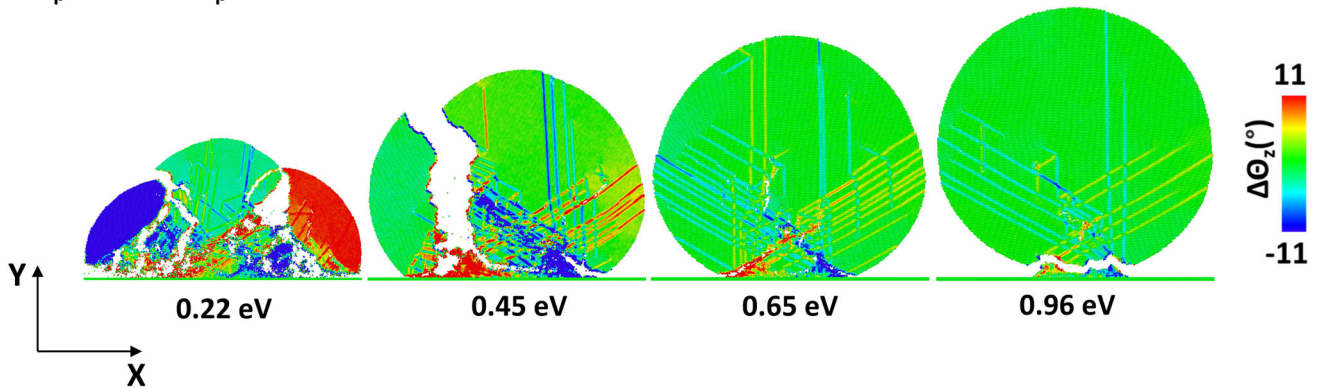


Fig. 14 Atomic rotation fields of 50 nm particles with different binding energies, 20 ps after collision with the velocity of 600 m/s. The crystallographic orientation of the particles was 30° tilted before impact to the substrates. Internal misorientation is indicated by

different color codes covering a regime between -11° and $+11^\circ$. Regions of the same color indicate grains, while straight lines correspond to the atomic rotation by shear strain and dislocations

d_p : 50 nm, average atomic shear strain: 0.2

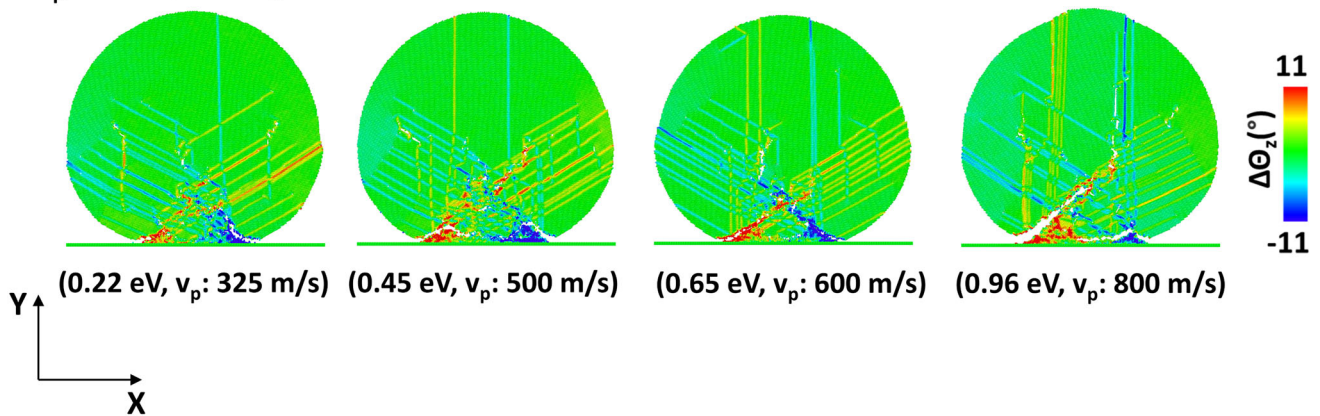


Fig. 15 Atomic rotation fields under the impact of 50 nm particles with different binding energies under tilted crystallographic orientation. Different impact velocities were applied to reach an average

atomic shear strain of 0.2 within the particles. The snapshots were taken 20 ps after the collision. The straight lines in color codes for rather low misorientation indicate shear strain and dislocations

d_p : 300 nm, v_p : 600 m/s:

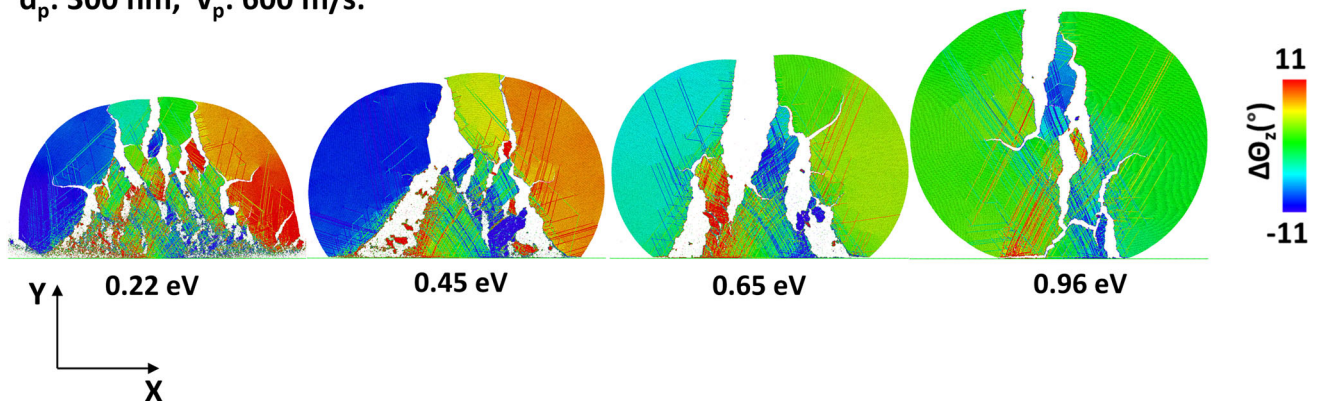


Fig. 16 Atomic rotation fields of 300 nm particles with different binding energies, 120 ps after collision with the velocity of 600 m/s. The orientation relation between particles and substrate was kept

epitaxial as Fig. 6 for 600 m/s. The straight lines in color codes for rather low misorientation indicate shear strain and dislocations

under a 30° tilt angle, Fig. 14 displays the atomic rotation fields of 50 nm particles that impacted the substrate with a velocity of 600 m/s. An impact velocity of 600 m/s was selected to study the grain refinement.

Examining the atomic rotation fields in Fig. 14 reveals two distinct types of fields. Distinct color codes were selected in order to cover a range of misorientations within a range from -11° to 11° . The straight-line fields represent the misorientation of atoms within the shear bands and dislocations. Similar colors indicate local regions with a common atomic orientational mismatch. Comparing regions of the same orientation, Fig. 14 indicates that the 50 nm particles with different binding energies show angular deviations and possible grain refinement mainly at the bottom at their interface to the substrates. At the given impact velocity of 600 m/s, the angular deviation is more prominent and stretches deeper into the interior for the cases of lower binding energies (0.22, 0.45 eV). For all investigated binding energies, grain refinement scales with the flattening along the interface to the substrate.

In order to ensure whether the observed grain refinement is mainly caused by the plastic deformation and fragmentation (as shown in Fig. 14) inside the particles, further studies were carried out for particles of different binding energies but same amounts of average shear strain. For the sake of simplicity and in order to match the obtained deformation results from Fig. 10, an average shear strain of 0.2 was selected. Figure 15 shows 50 nm particles that were first tilted by 30°, equilibrated at room temperature, and then collided to the substrate with different impact velocities. The resulting atomic rotation fields in Fig. 15 illustrate very similar atomic rotation patterns and consequently atomic rotation fields, despite the different binding energies and the different, respectively, needed impact velocities to gain an average shear strain of 0.2. Since particles with the same amount of deformation show very similar atomic rotation fields, it is reasonable to state that grain misorientation and possible refinement is caused by the plastic deformation inside the particles.

Atomic misorientation was also studied for the 300 nm particles in order to investigate whether particle sizes affect the degree of possible grain refinement. A previous study on AD of CeO₂ particles reported that grain refinement is (i) a precondition for successful film formation in AD and (ii) and prominently occurs when particles are larger than 200 nm (Ref 20).

In contrast with the 50 nm particles, where grain refinement was observed only for non-epitaxial impacts, the 300 nm particles exhibited grain refinement for epitaxial impacts, too. Therefore, each 300 nm single-crystalline particle was not tilted before the impact. Figure 16 illustrates the results of atomic rotation field studies in the 300 nm particles for different binding energies. Like for

the 50 nm particles, examining atomic rotation fields shows two distinct types of features: First, straight-line fields that correspond to the misorientation of atoms within the shear bands and dislocations. Second, regions in 2D show the same orientation and a distinct angular mismatch to the surroundings, corresponding to an atomic rotation angle or misorientation between -11° and 11° . Low-angle grain boundaries or sub-grain domains are usually those with a misorientation of less than about 11° . The lateral extension of one orientation is interpreted as an individual grain and considered a basis for observing grain refinement.

The examination of the atomic rotation fields within the 300 nm particles shows that misorientation is observed for the fragments and for varying extents at the bottom of the particles at locations of the highest shear strain. In some of these highly deformed regions, connected, distinct neighboring areas of different mean orientations are observed. This could be interpreted as grain refinement. Most of these areas still contain a high amount of shear lines. Thus, recrystallization within particles seems to be negligible at given modeling conditions and time scales. At given time scales, the observed grain refinement is probably attributed to local orientation changes under high shear strain.

The results in Fig. 16 illustrate those sizes of connected, individual orientations are one order of magnitude smaller than the original particle size. Derivable trends indicate that individual sub-structure sizes decrease with decreasing binding energies. Based on the modeling results from Fig. 14, 15 and 16, possible grain refinement in AD coatings could be caused by a combination of entrapping the fragments of particles and local misorientation under high shear strain.

Discussion

By applying MD simulations by using a simplified 2D model, the current approach aimed to derive more general trends for success in the aerosol deposition of ceramic materials with different properties. The results can support the selection of appropriate parameter sets with respect to needed particle velocities for coating formation. The investigated binding energies correspond to a range of YOUNG's moduli from 148 to 561 GPa. The different aspects of the influence of binding energies as the measure for material properties are discussed in the following.

Impact Behaviors

The deformation pattern under high-velocity impacts can be generally distinguished into phenomena of bonding, rebounding and fragmentation. In the case of small particle

sizes of 50 nm, all these different features are observed for all the investigated binding energies. However, velocities for reaching the transition regimes between them rise with increasing binding energies. Within the given binding energy range, MD simulations reveal an increase in threshold velocities for bonding from 200 to 600 m/s. This velocity range is rather similar to reported ranges of particle velocities in successful aerosol deposition of different ceramics (Ref 3). According to MD results of 300 nm particles, the transitions between the different phenomena are difficult to distinguish. At larger sizes, fragmentation already occurs within bonded particles. Related aspects based on local stresses and particle momentum were previously reported for a model material with properties similar to Anatase TiO₂ (Ref 8–10). The present study reveals that these findings may be generalized for a rather wide range of ceramic materials.

Threshold and Fragmentation Velocities

The presented MD simulations of 50 nm particle impact reveal that higher binding energies require higher threshold velocities for bonding. This relationship was observed across a range of binding energies, including artificial ceramics with YOUNG's moduli similar to silicon, titanium dioxide, alpha-alumina, up to tungsten carbide. The trend can be explained by considering that higher YOUNG's moduli lead to a need for greater external forces. These forces are required not only for causing elastic shear deformation but also for breaking local bonds during shearing, reaching the thresholds necessary to form dislocations.

Subsequent MD simulations of particles with different binding energies and diameters revealed that threshold velocities depend on binding energy rather than particle size. This agrees with the previous work describing an analytical model for the threshold velocity (Ref 10), which showed that the threshold velocity in AD is independent of particle size. From the consistency between present MD simulation results and the analytical description, it could be inferred that the threshold velocity range of 200–600 m/s generally applies to ceramic particles, irrespective of their micron or sub-micron sizes, and possibly the entire pre-conditions for the AD process. However, it should be noted that so far, reported experimental values for deposition by AD of 100–600 m/s (Ref 3) slightly exceed the derived threshold velocity range for ceramic particles of this study. This discrepancy can be attributed to the use of a simplified model and ideal and defect-free particles in the simulations. Any internal defect within real ceramics would allow for easier deformation.

As well as the threshold velocity, the fragmentation velocity also increases with binding energies. Stronger

bonds under higher binding energies also increase thresholds for breaking bonds, leading to crack formation. However, in contrast with the threshold velocity (v_{thre}), the fragmentation velocity (v_{frag}) strongly depends on the particle's size. For individual particle sizes, the fragmentation velocity rises with increasing binding energies, as illustrated in Fig. 8. The combination of threshold and fragmentation velocities allows for deriving a window of deposition. This window of deposition suggests that particles should be accelerated to velocities within the range of the threshold and fragmentation velocities to achieve the desired bonding behavior. Nonetheless, it must be noted that this obtained window of deposition should be only used for the interpretation of relative trends. Consecutive 3D studies and modeling of multiple particle ensembles would be required to derive concrete numbers and respective information on real coating formation.

Deformation Patterns

The simulated deformation patterns in 50 and 300 nm particles reveal that the plastic deformation occurring at the interface of the particle and substrate, seen in all rebounded, bonded or fragmented particles, and covering a wide range of binding energy, is most probably associated with the binding mechanism in AD. In the fragmented particles, the plastic deformations were mainly seen in the remaining triangle-shaped region on the substrate as characterized by the atomic shear strain fields stretching from the particle/substrate interfaces into the particles. These regions of high amounts of plastic deformation within the bonded or fragmented particles were mainly crack-free. The formation of such triangle-shaped crack-free regions that remained on the substrate after bonding and fragmentation is similar to the typically reported dense and pore-free coating morphology in AD (Ref 3, 4).

Nevertheless, the plastic deformation pattern reported in this study for a wide range of ceramic's binding energy is different from recent smooth particle hydrodynamic (SPH) simulations in 3D (Ref 5), where severe fragmentation was reported at the bottom of one micron-sized alpha-alumina particle at the interface of the particle with the substrate, while plastic deformation was seen at the top of the particles. On the one hand, these differences could be related to the size of the particle used in MD and SPH simulations. On the other hand, it should also be considered that when brittle material fracture is simulated via SPH, the fracture pattern will be dictated by the applied failure criteria in the SPH method (Ref 24) rather than the underlying interatomic interaction and lattice structure as in MD. Therefore, the cracks may not exhibit the same cleavage pattern as seen by MD, and the fracture might be more “smoothed out” due to the nature of the method.

Since plastic deformation is caused by shear strain in the particles along the slip system directions, the variation of average shear strain inside the 50 nm particle was studied for a wide range of impact velocities and binding energies (see Fig. 9). The correlation to impact velocities as the reason for overall loads underlines that the observed local deformation pattern scales with average shear strain, due to the importance of shear cracks and triangle-shaped regions in the deformation patterns of the bonded or fragmented features. Higher binding energies result in lower average shear strain. Particles with higher binding energies are less susceptible to deformation and shearing than those with lower ones. This is in accordance with mechanics since higher binding energies are associated with higher YOUNG's moduli. In building-up coatings, the adhering material will be hit by the following secondary particles. The loads under such secondary impact would probably cause fracture of pre-damaged adhering material. Thus, surpassing the threshold velocity might be viewed as the principal criterion for layer creation in AD. Given this context, particles with lower binding energy and, consequently, lower threshold velocities can offer a wider range of spraying velocities for successful deposition in AD.

Fragmentation Patterns

Studies of the deformation patterns of the 50 and 300 nm particles with different binding energies exhibit that (i) the meridional cracks forming at the upper part in parallel with the impact direction and (ii) the shear cracks forming at the boundaries of the triangle-shaped region are the main features for fragmentation. However, the individual amounts of cracks depend on the size of the particles, as well as on binding energy and loads by impact velocity. Shear cracks are more dominant in the 50 nm particles, while the meridional cracks, created by applying normal strains perpendicular to the impact direction, become more significant in the 300 nm particles (Ref 8). By increasing the binding energies, fewer shear cracks were observed in both the 50 and 300 nm particles.

In the 300 nm particles, the fragmentation is more severe than in the 50 nm particles. This could be attributed to the higher particles' kinetic energy and associated higher momentum and thus stress in the *X*-axis (Ref 8). As a result of increasing the binding energy in the 300 nm particles, a decrease in the number of shear cracks and an increase in the number of meridional cracks are observed.

Temperature Evolution

This study provides information on the mean and local temperatures within bonded and fragmented particles of different binding energies. The findings revealed that the

local temperature within the particles increases with impact velocity and binding energy, reaching up to 1800 K. The examination of local temperature fields revealed that higher temperatures occur within zones of maximum plastic deformation, i.e., triangle-shaped regions. Higher local temperatures are obtained for larger particle sizes, where heat diffusion pathways are too long for overall particle heating (Ref 10). This can be attributed to the fact that heat diffusion spreads with the square root of time, whereas the deformation shows a linear correlation (Ref 25). Also, local temperatures are higher in fragmented particles with higher binding energies. Such an increase could be attributed to the restrictions for the heat diffusion between the fragmented pieces.

Grain Refinement

The mechanisms behind grain refinement within AD coatings have not yet been fully understood (Ref 3, 20). The present study indicates that angular deviations in the orientation of 50 and 300 nm particles of different binding energies are seen mainly at (i) the fragmented pieces and (ii) within the triangle-shaped region at the bottom of the particles and their interface to the substrate. Whereas the sizes of the fragmented pieces are only slightly smaller than the original particles, an order of magnitude smaller grain sizes are only obtained within the shear cone areas. This observation agrees with transmission electron microscope observations from previous studies on AD ceramic coatings (Ref 3, 20). Furthermore, within both the 50 and 300 nm particles in this study, sufficient evidence was not found to establish whether a criterion should exist for refined grains, whether around 10–30 nm in size (Ref 2) or 200–400 nm (Ref 20), in the context of AD coatings.

The present study also shows that at a specific impact velocity, particles with higher binding energies lead to fewer fragmented pieces, but these fragmented pieces are larger in size as compared to the fragments of particles with lower binding energies. Therefore, a finer grain structure could be expected in the AD coating of particles with lower binding energies. Other potential mechanisms for grain refinement, like recrystallization, were not observed in this study, indicating a need for further investigations using more realistic crystal structures for each ceramic.

Summary and Conclusions

In this MD simulation study, a simplified 2D approach in terms of a modified Lennard–Jones potential was applied in order to model the high-velocity impacts of brittle particles with different binding energies. Despite the limitations of such simplification with respect to structural details, the

modeling results reveal general trends on influences of binding energies on the particle impact behavior in aerosol deposition. In detail, differences in (i) particle deformation and fragmentation, (ii) threshold and fragmentation velocities, (iii) temperature evolution and (iv) grain refinement are distinguished. The different conclusions from this work are summarized as follows:

1. Across a broad spectrum of binding energies in the developed artificial brittle particles, the threshold velocity is size-independent, while the fragmentation velocity demonstrated explicit particle size dependency.
2. Whole particle deposition, here defined as bonding, is expected if particle velocity is set between the threshold and fragmentation velocities.
3. Both threshold and fragmentation velocities increase with binding energies.
4. Particles with lower binding energy by smaller threshold velocities would allow for easier film formation in AD.
5. Grain refinement was seen by (i) plastic deformation at the triangle-shaped regions and (ii) by fragmentation of the particles into smaller fragmented pieces, which is more prominent for particles with lower binding energies.
6. Higher binding energies result in locally higher temperatures under shear deformation.
7. In the case of smaller particle sizes, heat diffusion leads to a more uniform temperature distribution.

The revealed trends supply a better understanding of the AD process and the individually needed conditions for depositing ceramic particles with different properties.

Acknowledgment B. Daneshian received funding from the Research Unit FOR 3022—Ultrasonic Monitoring of Fiber Metal Laminates Using Integrated Sensors—funded by the German Research Foundation (Deutsche Forschungsgemeinschaft (DFG)). W.E. Weber expressly acknowledges the financial support of the research work on this article within the project “KIBIDZ—Intelligente Brandgefahrenanalyse für Gebäude und Schutz der Rettungskräfte durch Künstliche Intelligenz und Digitale Brandgebäudezwillinge.” This project is funded by dtec.bw—Digitalization and Technology Research Center of the Bundeswehr within the framework of the European Union—NextGenerationEU. In addition, B. Daneshian, F. Gaertner and T. Klassen gratefully acknowledge financial support by the Federal Ministry of Education and Research (BMBF) of Germany given by the Project “FocusH2” (grant No. 03SF0479A).

Funding Open Access funding enabled and organized by Projekt DEAL.

Open Access This article is licensed under a Creative Commons Attribution 4.0 International License, which permits use, sharing, adaptation, distribution and reproduction in any medium or format, as long as you give

appropriate credit to the original author(s) and the source, provide a link to the Creative Commons licence, and indicate if changes were made. The images or other third party material in this article are included in the article’s Creative Commons licence, unless indicated otherwise in a credit line to the material. If material is not included in the article’s Creative Commons licence and your intended use is not permitted by statutory regulation or exceeds the permitted use, you will need to obtain permission directly from the copyright holder. To view a copy of this licence, visit <http://creativecommons.org/licenses/by/4.0/>.

References

1. J. Akedo, Aerosol Deposition Method for Fabrication of Nano Crystal Ceramic Layer, *Mater. Sci. Forum*, 2004, **449–452**, p 43–48. <https://doi.org/10.4028/www.scientific.net/MSF.449-452.43>
2. J. Akedo, Aerosol Deposition of Ceramic Thick Films at Room Temperature: Densification Mechanism of Ceramic Layers, *J. Am. Ceram. Soc.*, 2006, **89**, p 1834–1839. <https://doi.org/10.1111/j.1551-2916.2006.01030.x>
3. J. Akedo, Room Temperature Impact Consolidation (RTIC) of Fine Ceramic Powder by Aerosol Deposition Method and Applications to Microdevices, *J. Therm. Spray Technol.*, 2008, **17**, p 181–198. <https://doi.org/10.1007/s11666-008-9163-7>
4. R. Moos, An Overview of the Aerosol Deposition Method: Process Fundamentals and New Trends in Materials Applications, *J. Ceram. Sci. Technol.*, 2015, **6**(3), p 147–182. <https://doi.org/10.4416/JCST2015-00018>
5. H. Kwon, Y. Kim, H. Park, and C. Lee, Impact Behavior for Successful Particle–Particle Bonding in Vacuum Kinetic Spraying, *J. Therm. Spray Technol.*, 2020, **30**, p 542–557. <https://doi.org/10.1007/s11666-020-01078-7>
6. A. Elsenberg, T. Emmeler, M. Schieda, F. Gärtner, and T. Klassen, Tuning Aerosol Deposition of BiVO₄ Films for effective sunlight Harvesting, *J. Therm. Spray Technol.*, 2023, **32**, p 352–362. <https://doi.org/10.1007/s11666-023-01550-0>
7. B. Daneshian and H. Assadi, Impact Behavior of intrinsically Brittle Nanoparticles: A Molecular Dynamics Perspective, *J. Therm. Spray Technol.*, 2013, **23**, p 541–550. <https://doi.org/10.1007/s11666-013-0019-4>
8. B. Daneshian, F. Gaertner, H. Assadi, D. Hoeche, W. Weber, and T. Klassen, Size Effects of Brittle Particles in Aerosol Deposition—Molecular Dynamics Simulation, *J. Therm. Spray Technol.*, 2021, **30**, p 503–522. <https://doi.org/10.1007/s11666-020-01149-9>
9. B. Daneshian, F. Gaertner, W. Weber, T. Klassen, H. Assadi, and D. Hoeche, Molecular dynamics simulations of titanium dioxide as a model system for size effects in aerosol deposition, in *Proceedings of the International Thermal Spray Conference (ITSC 2021)*, May 24–28, 2021(virtual), ASM Thermal Spray Society, 2021, p 354–359. <https://doi.org/10.31399/asm.cp.itsc2021p0354>
10. B. Daneshian, F. Gärtner, H. Assadi, M.V. Vidaller, D. Höche, and T. Klassen, Features of Ceramic Nanoparticle Deformation in Aerosol Deposition Explored by Molecular Dynamics Simulation, *Surf. Coat. Technol.*, 2022, **429**, p 127886. <https://doi.org/10.1016/j.surfcoat.2021.127886>
11. H. Park, H. Kwon, Y. Kim, and C. Lee, Computational Research on Factors Affecting Particle Velocity in a Vacuum Kinetic Spray

- Process, *J. Therm. Spray Technol.*, 2019, **28**, p 1945-1958. <https://doi.org/10.1007/s11666-019-00941-6>
12. J. Henon, M.A. Piechowiak, O. Durand-Panteix, G. Etchegoyen, O. Masson, C. Dublanche-Tixier, P. Marchet, B. Lucas and F. Rossignol, Dense and Highly Textured Coatings Obtained by Aerosol Deposition Method from Ti_3SiC_2 Powder: Comparison to a Dense Material Sintered by Spark Plasma Sintering, *J. Eur. Ceram. Soc.*, 2015, **35**, p 1179-1189. <https://doi.org/10.1016/j.jeurceramsoc.2014.10.012>
 13. C.W. Kim, J.H. Choi, H.J. Kim, D.W. Lee, C.Y. Hyun, and S.M. Nam, Effects of Interlayer Roughness on Deposition Rate and Morphology of Aerosol-Deposited Al_2O_3 Thick Films, *Ceram. Int.*, 2012, **38**, p 5621-5627. <https://doi.org/10.1016/j.jeurceramsoc.2014.10.012>
 14. D.W. Davies, A.H. Moyers, M.D. Gammage, J.W. Keto, M.F. Becker and D. Kovar, Deformation and Film Formation Mechanisms During High Velocity Impact of Silicon Carbide Nanoparticles, *J. Aerosol Sci.*, 2022, **163**, p 105997. <https://doi.org/10.1016/j.jaerosci.2022.105997>
 15. A.H. Moyers, M.F. Becker, and D. Kovar, A Strain Density Function to Analyze Particle Size Effects During High Velocity Impacts of Ytria, *J. Am. Ceram. Soc.*, 2024, **107**, p 3925-3944. <https://doi.org/10.1111/jace.19708>
 16. A.P. Thompson, H.M. Aktulga, R. Berger, D.S. Bolintineanu, W.M. Brown, P.S. Crozier, P.J. in 't Veld, A. Kohlmeyer, S.G. Moore, T.D. Nguyen, R. Shan, M.J. Stevens, J. Tranchida, C. Trott, and S.J. Plimpton, LAMMPS—A Flexible Simulation Tool for Particle-Based Materials Modeling at the Atomic, Meso, and Continuum Scales, *Comput. Phys. Commun.*, 2022, **271**, p 108171. <https://doi.org/10.1016/j.cpc.2021.108171>
 17. T.A. Beu, *Introduction to Molecular Dynamics Simulations*, CRC Press, Boca Raton, 2023.
 18. S. Nosé, A molecular Dynamics Method for Simulations in the Canonical Ensemble, *Mol. Phys.*, 1984, **52**, p 255-268. <https://doi.org/10.1080/00268978400101201>
 19. A. Stukowski, Visualization and Analysis of Atomistic Simulation Data with OVITO—the Open Visualization Tool, *Model. Simul. Mater. Sci. Eng.*, 2009, **18**, p 015012. <https://doi.org/10.1088/0965-0393/18/1/015012>
 20. J. Exner, M. Schubert, D. Hanft, J. Kita, and R. Moos, How to Treat Powders for the Room Temperature Aerosol Deposition Method to Avoid Porous, Low Strength Ceramic Films, *J. Eur. Ceram. Soc.*, 2019, **39**, p 592-600. <https://doi.org/10.1016/j.jeurceramsoc.2018.08.008>
 21. S. Kuroyanagi, K. Shinoda, A. Yumoto, and J. Akedo, Size-dependent Quasi Brittle-Ductile Transition of Single Crystalline Alpha-Alumina Particles During Microcompression Tests, *Acta Mater.*, 2020, **195**, p 588-596. <https://doi.org/10.1016/j.actamat.2020.05.065>
 22. F. Shimizu, S. Ogata, and J. Li, Theory of Shear Banding in Metallic Glasses and Molecular Dynamics Calculations, *Mater. Trans.*, 2007, **48**, p 2923-2927. <https://doi.org/10.2320/matertrans.MJ200769>
 23. B. Daneshian, F. Gärtner, W.E. Weber, H. Assadi, and T. Klassen, The Impact of Binding Energies on the Necessary Conditions in Aerosol Deposition, *Proc. Appl. Math. Mech.*, 2023, **23**(3), p 1-7. <https://doi.org/10.1002/pamm.202300275>
 24. H. Assadi, H. Kreye, F. Gärtner, and T. Klassen, Cold Spraying—A materials perspective, *Acta Mater.*, 2016, **116**, p 382-407. <https://doi.org/10.1016/j.actamat.2016.06.034>
 25. W. Benz and E. Asphaug, Simulations of Brittle Solids Using Smooth Particle Hydrodynamics, *Comput. Phys. Commun.*, 1995, **87**, p 253-265. [https://doi.org/10.1016/0010-4655\(94\)00176-3](https://doi.org/10.1016/0010-4655(94)00176-3)

Publisher's Note Springer Nature remains neutral with regard to jurisdictional claims in published maps and institutional affiliations.